Assessment of earthquake locations in 3D deterministic velocity models: a case study from the Altotiberina Near Fault Observatory (Italy)

D. Latorre[1], F. Mirabella[2], L. Chiaraluce[1], F. Trippetta[3], A. Lomax[4].

[1] Istituto Nazionale di Geofisica e Vulcanologia, Roma, Italy.
[2] Dipartimento di Fisica e Geologia, Università di Perugia, Perugia, Italy.
[3] Dipartimento di Scienze della Terra, Sapienza Università di Roma, Roma, Italy.
[4]ALomax Scientific, Mouans-Sartoux, France.

Corresponding author: Diana Latorre (diana.latorre@ingv.it)

Key Points:

- 3D deterministic velocity models from combined high-resolution geological and geophysical data provide reliable earthquake locations
- Earthquakes located using these models allow a direct correlation between seismicity and geological structures
- The spatial correlation of earthquake locations with specific stratigraphic units suggests a lithological control on the seismic activity

Abstract

The accuracy of earthquake locations and their correspondence with subsurface geology depends strongly on the accuracy of the available seismic velocity model. Most modern methods to construct a velocity model for earthquake location are based on the inversion of passive source seismological data. Another approach is the integration of high-resolution geological and geophysical data to construct deterministic velocity models in which earthquake locations can be directly correlated to the geological structures. Such models have to be kinematically consistent with independent seismological data in order to provide precise hypocenter solutions. We present the Altotiberina (AT) seismic model, a three-dimensional velocity model for the Upper Tiber Valley region (Northern Apennines, Italy), constructed by combining 300 km of seismic reflection profiles, 6 deep boreholes (down to 5 km depth), detailed data from geological surveys and direct measurements of P- and S-wave velocities performed in situ and in laboratory. We assess the robustness of the AT seismic model by locating 11,713 earthquakes with a non-linear, global-search inversion method and comparing the probabilistic hypocenter solutions to those calculated in three previously published velocity models, constructed by inverting passive seismological data only. Our results demonstrate that the AT seismic model is able to provide higher-quality hypocenter locations than the previous velocity models. Earthquake locations are consistent with the subsurface geological structures and show a high degree of spatial correlation with specific lithostratigraphic units, suggesting a lithological control on the seismic activity evolution.

1 Introduction

Permanent seismic monitoring networks operate in real-time to gather fast and accurate information about the seismic activity of a target area. One of their first products is earthquake locations, routinely computed in one-dimensional (1D) models that are usually derived from simultaneous inversion of seismic velocities and hypocenter parameters [e.g., Kissling et al., 1994; Kim et al., 2006; among many others]. In these models, the velocity structure is parameterized by horizontal layers with constant velocities or increasing vertical velocity gradients. Although these kinds of models may give precise location results with small formal

uncertainties [e.g., Husen and Hardebeck, 2010], they may still represent a poor approximation of the Earth's structure in tectonically complex regions, thus potentially providing unreliable and biased earthquake locations.

An efficient approach to compute precise and accurate earthquake locations is solving the coupled inversion problem for velocity and hypocenter parameters in three-dimensions (3D). 3D velocity models from local earthquake tomography [e.g., Thurber, 1983] minimize systematic errors in earthquake location. Tomographic models are often obtained from special data sets recorded in limited periods of time. These models can be poorly constrained where ray coverage is not adequately dense or well distributed and, in some cases, provide an unrealistic image of the Earth's structure that is "filtered" and "averaged" by the chosen parameterization. Consequentely, while passive tomographic models are very useful for temporary studies of target regions, they are not always the best choice for routine earthquake locations of widespread background seismicity.

In conventional, passive seismic acquisitions, the sparse and nonuniform distribution of sources and receivers can reduce the capability of the tomographic inversion to resolve the trade-off between velocity and hypocenter parameters. In these cases, constraining the velocity model with geophysical and geological information can improve the accuracy of model and the hypocenter locations.

In the last two decades, the increased availability of subsurface data from geological and geophysical studies has allowed the construction of very detailed 3D velocity models for earthquake location. In some cases, controlled source seismic data are merged with passive tomographic models to constrain the structure of the main velocity discontinuities [e.g. Husen et al., 2003; Wagner et al., 2013]. In other studies, the seismic velocities from both commercial seismic lines and sonic logs [e.g., Cushing et al., 2008] or from passive tomographic inversion [e.g., Bethoux et al., 2016] are integrated into geological models to construct reliable velocity models. In northern California, the geological model of the San Francisco Bay area has been converted into seismic velocities by merging data from vertical seismic profiles (VSPs), sonic logs in boreholes, active and passive seismic studies, and laboratory measurements [Brocher, 2005]. This model, built for strong ground motion scenarios, has been also used for earthquake hypocenter locations [Lomax, 2008]. In all the aforementioned studies, location results have

shown that velocity models constrained by geological and geophysical data can provide greatly improved earthquake location solutions.

In approaches where earthquakes are located in seismological models, i.e., only constructed by inverting passive source seismological data, the correlation between the seismicity distribution and the geological structures is only analyzed "a posteriori" as part of a qualitative interpretation process. In the present work we follow a different approach by quantitatively evaluating whether the earthquake locations are consistent with the Earth's image defined by geological and geophysical data. We develop a deterministic seismic model in which the velocity distribution is constructed by merging geophysical and geological data, completely independent from passive source seismological data. Then, we investigate whether travel-times produced in such a model are able to provide reliable and high quality earthquake hypocenter solutions and consequently their direct correlation with the litho-geological structures.

The Upper Tiber Valley region in the Northern Apennines (central Italy) is an optimal framework to study hypocenter locations in 3D deterministic velocity models. Since 2010, this region hosts the Altotiberina Near Fault Observatory (TABOO, Chiaraluce et al., [2014]), a multidisciplinary research infrastructure that is providing a large amount of high-resolution geophysical data. We have developed a three-dimensional P- and S-wave velocity model (the AT seismic model) of the area by integrating a 3D geological model, which is based on deep boreholes data and about 300 kilometers of seismic reflection profiles [Mirabella et al., 2011 and reference therein], with sonic logs data and original laboratory measurements for different rock types [Trippetta et al., 2010, 2013a, 2015; Smeraglia et al., 2014].

In this work, we select 11,713 earthquakes recorded by the TABOO seismic network from April 2010 to December 2013, and we invert their hypocenters in the AT seismic model. We apply the non-linear earthquake location program NonLinLoc [Lomax et al., 2000], which is able to provide both hypocenter solutions in complex models and a comprehensive description of the location uncertainties. Then we analyze our results by comparing the quality of earthquake location solutions with those computed in three previously published velocity models, constructed by only inverting passive seismological data [Moretti et al., 2009; Carannante et al., 2013]. Finally we present the earthquake distribution in the tested velocity models and we

discuss the spatial correlation between the located seismicity and the main geological structures of the region.

2 Construction of the AT seismic model

The 3D seismic model of the Altotiberina region is a combination of two independent and complementary sets of geological and geophysical data. In this section, after a brief introduction of the tectonic setting of the region, we will detail both data and adopted strategy to construct the model.

2.1 Tectonic and structural style of the area

The study area is located in the Northern Apennines (Figure 1). It extends from the eastern border of the Val di Chiana basin to the Umbria-Marche inner ridge along the SW-NE direction [Scarsella, 1951], and from the San Sepolcro basin to Perugia city along the NW-SE direction, for a total extension of about 65 km x 55 km.

In the Umbria-Marche region, the complex tectonic architecture of the crust is the result of an earlier compressional tectonic phase (middle Miocene) and a subsequent extensional phase. This latter started in the upper Pliocene and is still active in the inner part of Apennines [e.g., Elter et al., 1975; Pialli et al., 1998; Barchi, 2010 and reference therein]. During the first tectonic phase, the Umbria-Marche sedimentary cover was deformed in east-verging folds and regional-scale thrusts. Compressional tectonics was responsible for crustal doubling as confirmed by surface and borehole data from the M. Civitello 1 and S. Donato 1 deep wells [Anelli et al., 1994], and observed in the seismic reflection profiles [Mirabella et al., 2011].

The later extensional phase displaced the Umbria-Marche compressional structure. Several geological and geophysical studies have demonstrated that a large part of the extensional deformation was driven by a 60 km long, ENE-dipping low-angle normal fault (the Altotiberina Fault, ATF), and a set of both synthetic (NE-dipping) and antithetic (SW-dipping) high-angle normal faults, located in the ATF hanging-wall volume [Boncio et al., 1998; Barchi 2002;

Mirabella et al., 2004; Collettini et al., 2005, among many others]. This fault system (Figure 1) generated the NW-SE-elongated structure of the Upper Tiber basin to the west and the Gubbio basin to the east [Pucci et al., 2014]. The Altotiberina fault borders the western part of the Tiber basin and reaches a depth of at least 12 km beneath the Umbria-Marche inner ridge [Mirabella et al., 2011]. The ATF has been recognized as one of the rare example of seismically active low-angle normal faults [Chiaraluce et al., 2007] and is still now the object of several geological and geophysical studies.

2.2 Geological and geophysical data

The starting three-dimensional geological model is based on geological and geophysical data analyzed in previous works to define the geological structure of the Upper Tiber Valley [Mirabella et al., 2004, 2008a, 2008b, 2011]. Data consist of geological maps, stratigraphy and sonic logs from boreholes, and seismic reflection profiles acquired for exploration purposes.

Surface data include geological maps of the Carta Geologica d'Italia (the Italian Geological Map, at 1:10,000, 1:50,000, and 1:100,000 scale), and maps from focused geological and structural surveys [Pucci et al., 2014]. Recent geological surveys were performed in the framework of the Geological Cartography Project and have given a great improvement in our knowledge of the extensional fault system of the Altotiberina region [Mirabella et al., 2011]

Subsurface data consist of seismic reflection profiles acquired by the Italian Oil Company Agip, presently Eni S.p.A., in the early 1980s. Eni oil company extensively explored the upper-crust structure of the Umbria-Marche Apennines through the drilling of six deep wells and the acquisition of about 40 seismic reflection lines, over 300 km long (Figure 1). In our target area, seismic reflection profiles clearly image the upper crust down to 4 s two-way time, which roughly corresponds to a depth of 10-12 km [Barchi et al., 1998c; Pauselli et al., 2002; Mirabella et al., 2008b]. In the last two decades, these reflection profiles were made available to the scientific community and represent the base for several studies [e.g., Barchi, 1991; Keller et al., 1994; Collettini et al, 2000; Mirabella et al., 2011]. During the mid '90, a near-vertical seismic reflection profile (the CROP-03) was acquired in the Northern Apennines, crossing the Upper Tiber Valley [Pialli et al., 1998]. The analysis of the CROP-03 seismic line allowed imaging the

164 Altotiberina fault as a part of a set of low angle detachments that accommodate the crustal
165 extension across the Northern Apennines [Barchi et al., 1998b; Boncio et al., 2000].

166 The six deep wells of the Eni oil company penetrate the Umbria-Marche stratigraphic sequence
167 down to a maximum depth of about 5 km. Figures 1a and 1c shows their location in map: the S.
168 Donato 1 (4,763 m b.s.l.) and the Perugia 2 (1,504 m b.s.l.) wells to the west, Pieve di Santo
169 Stefano 1 (4,936 m b.s.l.) to the north, Pratomagno 1 to the NW (4,259 m b.s.l.), Monte Civitello
170 1 (5,600 m b.s.l.) and Burano wells (2,494 m b.s.l.) in the central part of the area. Different
171 authors analyzed the data from these boreholes to interpret the seismic horizons observed in the
172 seismic reflection profiles [e.g. Bally et al., 1986; Barchi et al., 1998c; Mirabella et al., 2008a].
173 These authors identified the seismic signature of four main seismostratigraphic units that roughly
174 correspond to the major lithological groups of the Umbria-Marche stratigraphic sequence
175 (Figures 1b and 1d). Boundaries between these units are imaged in the seismic profiles with
176 continuous reflectors that can be clearly identified along neighboring seismic sections.

177 All the described geophysical data were analyzed by Mirabella et al. [2011] to compute depth
178 converted seismic profiles and build a geological model of the region. The seismic profiles
179 (Figure 1c) were collected to create a three-dimensional working project with the MOVE^{TM}
180 package, available from Midland Valley (http://www.mve.com/software/move). The 3D
181 architecture of seismic sections was constrained by both boreholes and surface geological data to
182 correctly account for datum shifts and crooked paths of the seismic lines. After the interpretation
183 phase, the seismic reflection horizons were converted to depth using seismic interval velocities
184 derived from both deep well data closest to the CROP 03 profile [Barchi et al., 1998a] and other
185 deep wells of the Central Apennines [Bally et al., 1986; Ponziani et al., 1995]. We started from
186 this 3D structure of seismic horizons to construct the layer geometries of the AT seismic model.

187

188 2.3 In situ and laboratory measurements of seismic velocities

189 Following the geophysical and geological setting described above, we define the sequence of
190 seismostratigraphic units characterizing the area (Figures 1 and 2). From bottom to top: (1) the
191 Paleozoic Crystalline Basement (CB), i.e., the deeper genuine crystalline basement of the Adria
192 Plate, (2) The Acoustic Basement (AB) composed by Paleozoic–Triassic clastic and meta-

193 sedimentary rocks, which represents the upper part of the Basement unit displayed in Figure 1b,
194 (3) the Triassic Evaporites (TE), (4) the Jurassic-Oligocene Carbonatic Multilayer (CM), and (5)
195 the Miocene Turbidites (MT), which include both the Miocene Umbrian turbidites and the
196 Miocene Tuscany turbidites.

197 Each stratigraphic unit assembles rock types that share similar lithologies and seismic properties
198 at large-scale. For most lithologies, we derive in situ measurements by first reanalyzing the deep
199 wells that drilled the upper four seismostratigraphic units of Figure 2, and then integrating well
200 data with the available literature data [Bally et al., 1986; Barchi et al., 1998c]. Borehole data
201 offer the advantage of being measured in situ with a proper scale. However, since they were
202 acquired in the 70's-80, S-wave velocity data are not available. Thus, to characterize both P- and
203 S-wave velocities, we benefit from laboratory measurements that offer a good control on the
204 boundary conditions, although they can be affected by scale problems due to the small
205 dimensions of the samples. We use published ultrasonic P and S-wave velocities measured at
206 elevated pressure (from 0 to ~300 MPa) and recorded with 1 MHz resonant frequency piezo-
207 electric transducers crystals on dry samples. By merging borehole and laboratory data, we have
208 assessed the proper P-wave and S-wave velocities for each seismostratigraphic unit, and
209 consequently the Vp/Vs ratio. To this aim we have calculated synthetic profiles of seismic P-
210 wave velocities at increasing depth assuming a stress gradient of 25 MPa/km, and rearranging
211 literature P-wave velocities data (Figure 2). These data have been compared with the Monte
212 Civitello deep borehole P-wave log, since it drilled through most of seismostratigraphic units of
213 the area. When laboratory measurements were measured at lower confining pressure respect to
214 the corresponding actual depth, we extrapolate the data to the higher pressures extending the
215 same trend registered for the last four measurements as suggested by Trippetta et al., 2010.

216 Hereafter, we illustrate the seismic velocities derived from borehole and laboratory
217 measurements (Figure 2). Then we introduce the velocities adopted for each seismostratigraphic
218 unit in the AT seismic model (Table 1).

219 The deepest part of the AT seismic model comprises the Crystalline Basement. Since no well
220 reached this basement, its lithological and geophysical characteristics have been inferred by data
221 from wells drilled in Tuscany that encountered mica schists and gneiss [Batini et al., 1983]. The

main data to infer its seismic velocity are the Deep Seismic Refraction (DSS) data [Ponziani et al., 1995; De Franco et al., 1998] that show an average velocity of 6 km/s. Laboratory measurements on analogue crystalline dikes outcropping at the Elba Island suggest P-wave velocities ranging from 4.6 to 5.8 km/s with increasing confining pressure [Burlini and Tancredi, 1998]. To model the P-wave velocities of the genuine crystalline basement, we refer to data coming from Burlini and Tancredi [1998]. Since in our model the basement is located at depths even higher than 7 km, the reference P-wave velocity value at high pressure (>175 MPa) is about 5.8 km/s. The adopted Vp/Vs ratio comes from literature data where there is a general agreement in considering 1.81 as a proper value for granitic rocks at high pressure [e.g. Jaeger et al., 2007; Wang et al., 2012].

Two deep wells, S. Donato 1 and Perugia 2, have drilled the upper part of the Acoustic Basement, represented by phyllites from the Upper Paleozoic age [Anelli et al., 1994; Ghelardoni, 1962]. Laboratory measurements on analogue phyllites and schists outcropping at the Elba Island suggest strongly anisotropic P-wave velocities ranging from 4.9 up to 5.9 km/s at 300 MPa [Burlini and Tancredi, 1998]. Literature data on similar rocks show a range of Vp/Vs spanning from 1.72 to 1.96 [e.g. Bostock and Christensen, 2012]. As well as for granites, we refer to Burlini and Tancredi [1998] for P-wave velocities of phyllites that are on average 5.3 km/s (red line in Figure 2) at depths greater than 4 km (~100 MPa). The adopted Vp/Vs ratio is 1.72 considering that the phyllites of the Altotiberina area seem to be more similar to samples C1 and C2 analyzed by Bostock and Christensen [2012].

Above the Acoustic Basement lies the Triassic Evaporites (TE) formation (Anidriti di Burano fm, Martinis and Pieri, [1964]). This is a 1 to 2 km thick sequence located between 2 and 5 km depth and composed by decimeter to decameter scale interbedded anhydrites and dolomites. Several boreholes drilled this formation both in the Northern and in the Southern Apennines, and show P-wave velocities ranging from 5.1 to 6.4 km/s [Bally et al., 1986; Barchi et al., 1998c]. Velocity frequency histograms of sonic logs recorded at three boreholes (Monte Civitello 1, San Donato 1 and Pieve Santo Stefano 1) show that the most registered velocities are 6.3 km/s for dolostones and 6.4 km/s for anhydrites [Trippetta et al., 2013a]. Average laboratory P-wave velocities are from 6.0 to 7.2 km/s for dolostones and from 5.8 to 6.3 km/s for anhydrites by increasing confining pressure from 0 to 100 MPa, in agreement with borehole data (Figure 2). In

the AT seismic model, the Triassic Evaporites are located at depths spanning from less than 1 km below the S. Donato 1 well up to 6 km in the eastern sector. By merging laboratory and borehole data and considering the large presence of fractured dolostones in the studied area, we assigned an average P-wave velocity of 6.3 km/s for this succession [Trippetta et al., 2013b; Carminati et al., 2013]. The average Vp/Vs ratio measured in laboratory is pressure independent being 1.76 for dry samples and increasing up to about 2.2 for fully saturated samples [Trippetta et al., 2010]. Since fluids are surely present at depth we used an average value of 1.83 (red line in Figure 2c).

The lithostratigraphic position of the Carbonatic Multilayer is indicated in Figure 2a. It is constituted by lower-Lias platform carbonates (the "Calcare Massiccio" fm) and a pelagic carbonate sequence (the "Scaglia") made up of basinal cherty limestone and intercalated marly formations. The thickness of the entire unit ranges between 1 and 2.5 km. The average velocity of the whole Carbonatic Multilayer from borehole measurements is about 5.6 km/s (Figure 2). Recent laboratory measurements of the Calcare Massiccio fm coming from the same area show pressure independent velocities of 6.0-6.1 km/s [Trippetta et al., 2015]. Taking into account that marly levels are present within this Carbonate Multilayer, we estimate that a P-wave velocity of 5.7 km/s represents a good match between borehole measurements and laboratory data for the whole thickness (red line in Figure 2b). The average Vp/Vs ratio measured in laboratory is 1.74 for dry samples and about 2.0 for saturated samples, while both are pressure independent. The chosen Vp/Vs ratio is 1.9 since fluids have been recorded in all the wells that drilled this unit (red line in Figure 2c). This value is in agreement with other measurements of P- and S-waves in limestones from full waveform sonic logs [e.g., Miller and Stewart, 1990] and several tomographic studies performed along the Northern Apennines [e.g., Chiarabba et al., 2010; Di Stefano et al., 2011].

The turbidites deposits are indicated as Umbria Turbidites (Early Late Miocene) by Mirabella et al. [2011]. They are mainly constituted by sandstone and marls, and spans from the surface to about 3 km depth. Recent laboratory measurements on turbidites coming from the Central Italy show a large range of P-wave velocity values from a minimum of 1.5 km/s at ambient pressure up to 4.5 km/s at 100 MPa of confining pressure [Smeraglia et al., 2014]. Velocity measurements on this unit show clear pressure dependence, especially for the first 40 MPa of applied confining pressure corresponding to about 1.5 km of burial (Figure 2). From 0 to 40 MPa the increase in

velocity is very large, meaning that at very shallow depth the P-wave velocity of this succession is severely increased with respect to the starting one. In choosing the best P-wave velocity for the Miocene Turbidites we take into account that this formation is characterized by the more pressure sensitive P-wave velocity of the involved seismotectonic units. Since in our model the Miocene Turbidites are located up to 3 km at depth we adopte a P-wave velocity of 4.0 km/s (red line in Figure 2b). The average Vp/Vs ratio measured in laboratory is 1.5 for dry samples and about 1.9 for saturated samples, while both are pressure independent [Smeraglia et al., 2014]. Due to the presence of fluids also within this formation we have chosen a Vp/Vs ratio of 1.8.

Table 1 summarizes the seismic velocities collected for each unit of the AT seismic model. The five lithostratigraphic groups of the area are listed in the first column. In the second and third column we report two sets of P-wave velocities from two different analyses. The first one includes the average interval P-wave velocities used to convert to depth the seismic horizons that define the geometry of the AT seismic model. The second set includes the average P-wave velocities that we have obtained by combining in situ and laboratory measurements. In the last column we show the average Vp/Vs ratios derived from laboratory measurements and literature data. Comparing the two P-wave velocity data sets we observe that they are in very good agreement with each other. Differences are very small (less than 4.0 %) taking into account that we are considering average P-wave velocities of lithological groups over a large scale (tens of kilometers). The compatibility between P-wave velocities from independent studies allow us to merge and test them in the AT seismic model.

2.4 The final AT Seismic Model

The AT seismic model is composed of velocity layers which have laterally varying thickness and represent the spatial distribution of the main stratigraphic units (Table 1). To construct the model, we interpolate the 3D architecture of depth converted horizons identified in the previous study of Mirabella et al. [2011]. For the interpolation process we used the GOCAD software package that runs the Discrete Smooth Interpolation algorithm conceived to model complex geological surfaces [Mallet, 1989, 1992]. The 3D structures of interpolated seismic horizons represent the velocity layers boundaries of the AT seismic models.

311 Since most of the seismic horizons are well imaged in the seismic reflection profiles, their
312 associated lithostratigraphic units are well constrained in the geological model. Only the base of
313 the Acoustic Basement over the Crystalline Basement is not clearly imaged. Therefore, we
314 modeled this deeper interface by assuming a constant layer thickness. According to literature
315 data [Ponziani et al., 1995; De Franco et al., 1998] we generated the bottom-level interface by
316 using the top of the Acoustic Basement as a template and setting a vertical thickness of 2 km.
317 This thickness was estimated from refraction DSS data [Ponziani et al., 1995], from few well-
318 data that penetrated similar rocks in other parts of Italy [e.g., Bally et al., 1986; Patacca and
319 Scandone, 2001], and from the size of the low-wavelength reflections that are visible on the
320 seismic reflection profiles.

321 After defining the geometry of the model layers, we associated the P- and S-wave velocities to
322 each unit, starting from the data shown in Table 1. We assume that the velocities are constant in
323 each layer, representing the average velocity values for each lithostratigraphic unit.

324 In order to adopt the best combination of seismic velocities, we have tested the two sets of P-
325 wave velocities reported of Table 1. To this end, we have constructed two versions of the AT
326 seismic model, with different P-wave velocities but the same Vp/Vs ratio, being the latter only
327 constrained by laboratory data and scaled following the sonic logs information. In Model 1 we
328 include the set of P-wave velocities from in situ and laboratory measurements. These velocities
329 are consistent to the Vp/Vs ratio but are uncorrelated to the geometries of the velocity layers,
330 since they come from different studies. In Model 2, we adopted the P-wave velocities used to
331 convert to depth the seismic horizons defining the layer geometries. Velocities from laboratory
332 measurements are integrated in Model 2 through the Vp/Vs ratio. Although P-wave velocities
333 from laboratory are not directly included, however this second model guarantees a more robust
334 consistency between layer geometries and seismic velocities derived from laboratory
335 measurements. To test the model performance, we located a selected data set of 3,274
336 earthquakes using the NonLinLoc program (see Figure S1 and related discussion in the
337 supplementary material). Our test shows that the quality of the location solutions in the two
338 models is very similar, despite a slightly lower travel time residuals for Model 2. Since the two
339 models can be considered equivalent in term of travel time residuals, we have chosen to adopt

Model 2 for the AT seismic model, since it better reconciles seismic reflection data, in situ and laboratory measurements, and seismological data.

Figure 3 summarizes the construction of the AT seismic model. From top to bottom, are displayed: two time-migrated seismic sections along the S3 profile (Figure 3a), the vertical cross-sections of the 3D geological model from Mirabella et al. [2011] along the same profile (Figure 3b), the geometry of the main structural units as defined in the present study from depth conversion of seismic reflection horizons (Figure 3c), and the AT seismic model (Figure 3d).

The AT seismic model is parameterized by a velocity grid of 650 x 550 x 220 cubic cells, of side 100 m for a total extension of 65 km x 55 km x 22 km. We have chosen this grid size because it allows us to adequately compute seismic wave travel-times with the finite-difference algorithm of the location procedure.

The model contains complex lateral and vertical variations of seismic velocities that strongly affect the propagation behavior of the seismic waves and, consequently, the computed first-arrival travel times directly involved in the earthquake location procedure. To simulate these propagation effects, we have chosen a theoretical source located along the deeper part of the Altotiberina fault (yellow star in the Figure 3). Then, we have computed the P-wave travel-times using the Eikonal finite-difference scheme of Podvin and Lecomte [1991]. The travel-time wavefronts, represented by isochrones in Figure 3d, appear strongly deformed where the velocity contrast between the units is higher, as for example along the contact between the Triassic Evaporites and the Acoustic Basement. Wavefront deformation is enhanced below the S. Donato 1 well where the Triassic Evaporites reaches very shallow depths due to a doubling of the structural units. The Altotiberina fault, as defined by the analysis of seismic reflection profiles [Mirabella et al., 2011], cuts the entire AT seismic model. In some cases, the ATF corresponds to the boundary between stratigraphic units, and then represents the interface of high velocity contrasts that produce in our modeling deformations of the wavefront geometry. In other cases, the ATF crosses the stratigraphic units and its presence does not produce changes in the waveform propagation since possible related velocity contrasts, presumably represented by the fault zone, are not included in our model in reason of their small dimension [i.e., meters scale, Smith et al., 2008].

3 Earthquake locations in the Altotiberina seismic model

We compare the AT seismic model constructed with independent geophysical data with previous models based on earthquake phase picks. We focus on wave propagation effects in term of travel times, by inverting in the AT seismic model a set of observed P- and S-wave first-arrival times to produce earthquake hypocenter parameters. We invert the same set of travel times in three different velocity models constructed in previous seismological studies [Moretti et al., 2009; Carannante et al., 2013]. Then, we perform a comparative analysis of the retrieved location solutions. The AT velocity structure will also produce strong effects on the seismic wave amplitudes as well as secondary waves scattering, however the investigation of these effects is not in the aim of the present study.

3.1 Data selection

To test our model, we selected a set of earthquakes recorded from April 2010 to December 2013 by the TABOO seismic network and by stations of the Italian National Network, both managed by the National Institute of Geophysics and Volcanology. The network configuration (Figure 4a) covers an area of 120 x 120 km^2 and is composed of 51 permanent stations equipped with three-component sensors having a sampling rate of 0.01 s.

Continuous seismic records are processed with an automatic procedure providing earthquake catalogues of hypocenter locations in near real-time [Di Stefano et al., 2014]. In this procedure, an automatic picking algorithm called MannekenPix [MPX; Alderson, 2004; Di Stefano et al., 2006] identifies P- and S-wave arrival times while assessing their quality with an "a-priori" weighting scheme. Although MPX does not include a systematic manual inspection of the waveforms, it provides high-quality picks for a large amount of data while avoiding data inconsistencies since it is based on uniform picking weight assignments [Di Stefano et al., 2006]. In our location procedure, we avoid possible problems of outlier data related to the automatic picking by using the Equal Differential Time (EDT) likelihood function [Font et al., 2004]. This

function is very efficient in the presence of picking outliers and is included in the earthquake location program NonLinLoc [Lomax et al., 2000, 2009].

From April 2010 to December 2013, the automatic procedure has identified about 86,000 earthquakes [Di Stefano et al., 2014]. In this work, we focused on two subsets of this catalogue. Since we want to analyze only arrival times whose theoretical propagation occurs inside the 3D model, we performed a preliminary earthquake location with the NonLinLoc program using an available regional 1D velocity model of the Umbria-Marche region [Carannante et al., 2013]. Then, we excluded all the seismic stations and earthquakes located outside the AT seismic model boundaries.

We have constructed two pick data sets to serve different purposes. In a first case, we include only very high quality picks in order to insure that discrepancies between earthquake locations obtained in different velocity models were less dependent on picking errors and mainly related to the velocity models adopted in the inversion process. This selection helps us to perform a quantitative comparison between different location solutions. In a second case, we applied a less restrictive picking quality selection in order to increase the number of earthquakes and have a larger event distribution in the entire target volume.

The first data set includes only P- and S-wave readings with Gaussian uncertainties (standard deviations) from 0.025 to 0.1 seconds, corresponding to a range of picking weight codes from 0 to 2. Weight codes define the weight applied to the phase reading in the inversion process, from full use (0 or full weight) to not use (4 or no weight). S-wave readings were retained only if coexisting with P-wave pickings that respect our weight limits. We selected all the events that have at least 14 P- and 7 S-wave picks. Thus, 3,275 earthquakes with 58,134 P- and 39,271 S-wave arrival time observations compose the first higher-quality data set whose location is shown in Figure 4 (black dots).

The second data set includes events with at least 8 P- and 5 S-wave readings. Gaussian uncertainties are lower than 0.2 seconds, corresponding to a picking weight code that ranges from 0 to 3. With respect to the first data set, the number of selected earthquakes increases to 11,713, covering a larger area and including more events located along the Altotiberina fault (gray dots in Figure 4b).

425

426 3.2 Earthquake location method

427 In strongly heterogeneous velocity structures, earthquake location inverse problems can be
428 highly non-linear and ill-conditioned, implying very complex solutions. In these cases, direct,
429 global-search methods are more suitable to provide complete location solutions. Due to the
430 complex velocity architecture of the AT seismic model, we have chosen to compute hypocenter
431 locations with the inversion program NonLinLoc [Non-Linear-Location, hereafter NLL, Lomax
432 et al., 2000], that is based on a probabilistic earthquake location approach [Tarantola and
433 Vallette, 1982; Moser et al., 1992], and includes a comprehensive estimate of the location
434 uncertainties. NLL uses the travel-time computation algorithm of Podvin and Lecomte [1991]
435 based on the Eikonal finite-difference scheme, and the Oct-tree importance sampling inversion
436 algorithm. Both these algorithms are very efficient for complex 3D models.

437 In the last decades, the NLL program has been successfully applied in many geological contexts
438 [Lomax et al., 2001; Husen et al., 2003; Husen and Smith, 2004; Lomax 2005, 2008; Cushing et
439 al., 2008; Korger and Schlindwein, 2012, among many others]. For a detailed description of the
440 NLL program, we refer to Lomax et al. [2000, 2009] while we report hereafter some basic
441 concepts.

442 Following the probabilistic formulation of Tarantola and Vallette [1982], the hypocenter location
443 is expressed by the a posteriori probability density function (PDF), which represents a function
444 of the probability distribution over all the possible spatial hypocenter locations. This function
445 contains an estimate of the location uncertainty that depends on many factors, such as the spatial
446 relation between the receiver network and the earthquake position, the uncertainty in the
447 observed arrival times, and the travel-time errors. The latter uncertainty partly depends on the
448 chosen velocity model and its accuracy.

449 In practice, we indicate the maximum likelihood point of the computed PDF as our “optimal”
450 earthquake hypocenter location. In simplified cases, when the hypocenter location problem is
451 well constrained by the available data, or it is not ill-conditioned due to the complexity of the
452 velocity model and travel-time field, the PDF forms a near-ellipsoidal shape and contains a
453 single maximum likelihood point. However, when the location is not well constrained, the PDF

454 representation can have irregular form with multiple, local maximum likelihood points
455 [Tarantola and Vallette, 1982].

456

457 3.3 Location quality assessment

458 In order to validate the capability of the AT seismic model to provide precise and accurate
459 hypocenter locations, we have inverted the selected data sets in our model and in three velocity
460 models of the Altotiberina region constructed with passive seismological data (Figure 5). Two of
461 these models (Figures 5b and 5c) were obtained by Moretti et al. [2009] in a tomographic study.
462 The authors inverted 1,159 earthquakes recorded during a temporary seismic experiment carried
463 out in 2000-2001 [Piccinini et al., 2003]. The first model (hereafter 3D-Tomo, Figure 5b) is a
464 local 3D tomographic model computed with the SIMULPS code [Thurber 1983], which provides
465 a distribution of P-wave velocities and Vp/Vs ratio linearly interpolated over a tri-dimensional
466 grid. The second model (hereafter 1D-Layer, Figure 5c), which was developed using the
467 VELEST code [Kissling et al., 1994], presents a 1D structure with constant P-wave velocities in
468 each layer and a constant vertical Vp/Vs ratio. The third model (hereafter 1D-Grad, Figures 5d)
469 is parameterized by vertical gradients of P-wave velocities and vertical varying Vp/Vs ratios. It
470 was computed by Carannante et al. [2013] with the VELEST code [Kissling et al., 1994] and
471 used as reference velocity model for a regional scale tomographic study. For our study, we
472 converted all the models in a 3D grid of cubic cells, identical to that adopted for the AT seismic
473 model (Figure 5a).

474 To provide a visual comparison of the wave propagation effects, we have plotted in Figure 5 the
475 P-wave travel-time field calculated in each model with the finite-difference algorithm of Podvin
476 and Lecomte [1991]. All the models reveal different shapes of travel-time wavefronts that can
477 strongly affect the hypocenter location results. With respect to the other velocity structures, the
478 AT seismic model presents more pronounced propagation complexities. In contrast, although the
479 3D-Tomo model includes lateral velocity heterogeneities, P wavefronts assume smooth shapes
480 similar to the 1D-Grad model, since the tomographic model parameterization linearly
481 interpolates the velocities over a coarse grid of nodes (3.0 km spaced in depth). The 1D-Layer
482 model images the velocity inversion located at 5-6 km depth and documented in the Monte

Civitello 1 sonic log (Figure 2). Nevertheless, the unrealistic lateral extension of this velocity contrast in a 1D structure produces head waves that follow very different paths with respect to the AT seismic model.

The four velocity models shown in Figure 5 are used to locate the selected 3,275 events with the NLL code. The quality estimates of the obtained hypocenter solutions are summarized and compared in Figures 6 and 7.

Figure 6 illustrates the agreement between observed and computed travel times. We show the root-mean-square (rms) of each location solution, i.e., the weighted, root-mean-square of the first-arrival residual times computed at each maximum-likelihood hypocenter, and the distribution of the P- and S-wave residual times. In each panel, we compare the location results obtained in the AT seismic model with respect to those computed in the 3D-Tomo model (Figure 6a), the 1D-Layer model (Figure 6b), and the 1D-Grad model (Figure 6c). For this comparison, we did not include any data quality selection after hypocenter location. Thus, plots illustrate how the different propagation models agree with the entire set of observations.

All tested velocity models provide hypocenter locations with low rms values (<0.15 s). The average rms calculated for all solutions ranges from 0.064 s (AT-seismic model) to 0.084 s (1D-Layer model). The hypocenters located in the AT seismic model presents an overall quality improvement of formal location errors expressed as mean rms reduction of about 11% over the 1D-Grad model, 12% over the 3D-Tomo model, and 23% over the 1D-Layer model. The distribution of the rms in the first plots (a1, b1 and c1 of Figure 6) visually show that a majority of the location solutions in the AT seismic model exhibits lower rms than the other models.

A different view of the rms results is displayed by histograms in the a2, b2, and c2 plots (Figure 6). They indicate that the rms distribution of the hypocenter solutions in the AT seismic model are shifted toward lower values than the solutions in the other velocity models. The bell-shaped distribution is similar to that of both the 3D-Tomo and 1D-Grad models, while it is larger in the 1D-Layer model with associated higher rms values. The last two histograms display the residual time distribution of 58,134 P- and 39,271 S-wave picks (plots a3, b3, c3 and a4, b4, c4 of Figure 6). Blue bins indicate the residual times calculated at the maximum-likelihood hypocenters in the AT seismic model while red bins correspond to the distribution of the hypocenters located in the

512 other velocity models. Details of the mean values and standard deviations (std) for each
513 distribution are reported in the figure.

514 We observe a good match between P-wave residual times calculated in the AT seismic model
515 and those computed in the two models from Moretti et al. [2009] (Figure 6a and 6b). This
516 agreement (mean P-residuals value < 0.010 s) is probably related to the construction of these
517 models, also being constrained by borehole data from the M. Civitello 1 well, which is located in
518 the center of the AT-seismic model and whose data were also included in the construction of our
519 velocity model. On the contrary, the 1D-Grad model, which did not include local geological
520 constrains, presents a greater mean value (0.026 s) of P-wave residual times.

521 The results are different in the case of the S-wave residual-time distributions. Firstly, the
522 hypocenter locations in the AT seismic model still provide lower S-wave residual times, with a
523 mean value close to zero (0.010 s) and low standard deviation (0.221 s). This result supports our
524 setting of Vp/Vs parameters from laboratory data. Secondly, the two models from Moretti et al.
525 [2009] show a clear asymmetric distribution of the S-wave residuals with prevalent negative
526 values, indicating that the computed S-arrival times have been underestimated. On the contrary,
527 since the 1D-Grad model was constructed with vertical varying Vp/Vs, it is able to reproduce the
528 S-wave arrival times. General standard deviation of S-residual distribution ranges from 0.221 s
529 to 0.244 s in the AT seismic model and in the 1D-Layer model, respectively. Overall, the AT
530 seismic model fits better the majority of the P- and S-wave time observations respect to the other
531 models, suggesting the goodness of both our geometry reconstruction of the lithological bodies
532 and our choice of the seismic velocities.

533 In Figure 7 we present the uncertainties of the hypocenter location solutions. The PDF volume
534 gives us an estimate of the earthquake location uncertainty since it measures the extension of the
535 high likelihood region of the probability density function. However, since Gaussian estimators of
536 the location uncertainty may be computed from the PDF, we also describe more traditional
537 quantities, such as the 68% confidence ellipsoid of the error that is computed from the
538 covariance matrix at the expectation hypocenter location, i.e., the Gaussian statistic hypocenter
539 location [Lomax et al., 2000]. Gaussian estimators of uncertainties are a good approximation of
540 the spatial error only in the case where the complete, non-linear PDF has a single maximum and
541 ellipsoidal form. When this case is verified, the maximum likelihood location is close to the

expectation hypocenter location.

As in Figure 6, we display in Figure 7 three panels where the uncertainty estimators of the hypocenter solutions computed in the AT seismic model are compared to those obtained in the others velocity models. Histograms show data distributions with shape skewed toward the lower values. In some cases (e.g., the PDF volume) their shape is close to a log-normal distribution. However, for simplicity in this study we estimate the median value which is generally the best representative parameter of data with such skewed distributions. In order to verify if we can correctly compare these data distributions with each other, i.e., whether the distributions are different or representative of the same population, we checked our results by applying the non-parametric test of Wilcoxon (the Wilcoxon rank sum test, Gibbons and Chakraborti [2011]), which is valid for data with a generic distribution. Since we obtain very low p-values (probability of null hypothesis lower than 0.01) for each couple of distributions, we suggest that the sampled data presented in our study are representative of different populations, and then we can reasonably compare their representative median values.

Hypocentral solutions obtained in all the tested velocity models provide very small PDF volumes (median values lower than 0.130 km^3) suggesting that our data selection criteria have brought to well resolved earthquake locations (graphics a1, b1, and c1 of Figure 7). Hypocenter solutions in the AT seismic model exhibit the smallest PDF's volumes with a median value of 0.074 km^3 and a median reduction that ranges between 23% (3D-Tomo model) and 43% (1D-Layer model). This evidence indicates that the hypocenter solutions in the AT-seismic model have, on average, higher resolution and lower location uncertainties than the other tested models.

Although the distance between the maximum likelihood hypocenter and the expectation hypocenter location varies widely (graphics a2, b2 and c2), it globally shows relative low values, close to the size of our inversion grid (median values from 0.144 km to 0.219 km). This implies that most of the PDF hypocenter solutions have a quite regular form, with a single maximum likelihood point. In these cases, if we approximate the PDF shape with an ellipsoidal form, we can use the Gaussian location error estimators, as for example the semi-axes of the 68% confidence ellipsoid, for comparison between our location solutions. We choose an arbitrary threshold of 0.5 km, which is 5 times our inversion grid size, to select only the hypocentral solutions with small distance between the maximum likelihood and the expectation hypocenter

location. For these selected events, we plot the distributions of the horizontal and vertical errors computed at the 68% confidence ellipsoid (Figures 7). Information from these Gaussian uncertainties is in agreement with the analysis of PDF's volume estimator. This shows that hypocenter solutions in the AT seismic model are characterized by lower spatial errors than other solutions, having median horizontal and vertical uncertainties of 0.262 km and 0.746 km, respectively.

3.4 Location results

After assessing the quality of the hypocenter solutions, we visually analyze whether the seismicity distribution is consistent with our knowledge of the geologic structures of the study area. For this analysis we located the largest selected data set composed of 11,723 earthquakes. In Figure 8 we display the hypocenters computed in all the tested velocity models along a set of vertical cross-sections. Map views of the earthquake locations are presented in the supplementary material (Figure S2). Vertical cross sections, whose position in map is shown in Figure 4, are chosen perpendicular to the NWW-trending Altotiberina normal fault and its system of synthetic and antithetic faults.

Our first important result is the general agreement between earthquake locations obtained in the AT seismic model and in the other seismological models. This conclusion is not obvious considering that the AT seismic model was not at all constrained by passive seismological data. We clearly identify seismic activity along the low-angle structure corresponding to the Altotiberina fault, from about 4 km down to about 13 km of depth. The ATF foot-wall is almost aseismic while its hanging-wall is interested by an intense activity mainly confined within the upper 5 km of the crust.

In detail, the seismicity following the ATF geometry is well delineated in Sections 1 and 2. In the AT seismic model the earthquake distribution defines a low-angle dipping plane better than earthquakes located in the other velocity models. Section 1 shows that isolated shocks scattered in the seismological models beneath the Gubbio fault are instead well concentrated in the AT seismic model. Here, either they assume the shape of very small clusters in the upper 6 km of the crust, or they are shifted in depth to define a northeastern dipping structure. It is interesting to

note that the deepest earthquakes (10-13 km) located nearby the easternmost termination of the ATF, show an opposite SW-dipping trend. Such feature is not an artifact of our model since it is in agreement with the seismicity pattern retrieved in all the velocity models.

Section 3 displays only a small subset of earthquakes that follows the ATF structure. These earthquakes appear very well clustered in the AT seismic model and occur where the ATF trace marks the velocity contact between the Acoustic Basement and the Crystalline Basement. On the contrary, earthquakes are spread over a larger volume in the other models since they do not include such a sharp velocity change. The reliability of the retrieved seismicity pattern in the AT seismic model is suggested by the evidence that similar alignments are also found where the ATF does not correspond to a velocity contrast in our model, as shown in Section 1.

Earthquakes located in the hanging wall of the Altotiberina fault are mainly displayed in cross sections 2, 3 and 4. In particular, Section 2 shows part of the seismic sequence that started at the end of 2013, with a maximum magnitude of M_W3.9 (the Gubbio event of December 22 2013, Figure 4) and normal fault focal mechanism [http://cnt.rm.ingv.it/tdmt]. In Section 3, the seismicity includes a small seismic sequence that occurred near the town of Pietralunga (Figure 4) with events up to a maximum magnitude of M_W3.6 (the Pietralunga event of April 15 2010). Section 4 presents the seismic sequence occurred near the town of Città di Castello after the Mw 3.6 earthquake of May 8 2013. The main event of this sequence also exhibits a normal fault focal mechanism [http://cnt.rm.ingv.it/tdmt].

In all these sections we observe that the upper (5-6 km depth) seismicity is still more clustered in the AT seismic model, while earthquakes are more diffuses over larger volumes in models that do not take into account the lateral velocity heterogeneities. In the case of the Gubbio sequence (Sections 2) the seismicity located in the AT seismic model collapses within a volume whose shape is compatible with the presence of secondary synthetic and antithetic high-angle faults delimiting a zone with a high seismic activity. The shape of this zone is consistent with the hypocenter locations computed in the 3D-Tomo model, although in this latter the seismicity image is more diffuse. Similarly, in the Pietralunga area the AT seismic model and the 3D-Tomo model show similar seismicity patterns while they are different from both the 1D velocity models, demonstrating that lateral velocity changes of this complex geological context play an important role in hypocenter locations.

One of the strongest differences between the hypocenter distributions is observed near the town of Città di Castello, located in the northwestern part of the region (Section 4). In both the 1D-Grad model and the 3D-Tomo model, the seismicity pattern presents a pipe-like form, about 8 km long and distributed along a vertical orientation. This elongated shape is most likely an artifact of the smooth vertical variation of the velocity models combined with their low resolution in this area. On the contrary, the 1D-Layer model presents a well clustered seismicity, which is divided into two distinct and unrelated clusters located under and beneath the Altotiberina fault. A more realistic seismicity pattern is obtained in the AT seismic model where earthquakes are well clustered in a unique small volume, located in the hanging wall of the Altotiberina fault. Both geometry and location of the cluster are consistent with the Time Domain Moment Tensor (TDMT) focal mechanism computed for the larger (M_W3.6) event of the sequence and the behavior of the other small seismic sequences that occur along high-angle normal faults in the hanging wall volume of the Altotiberina fault [e.g., Boncio et al., 2000; Chiaraluce et al., 2007].

In order to discuss the effectiveness of the AT seismic model in properly reconstructing the seismicity distribution at small scale, we display in more detail the hypocenter locations of 613 earthquakes belonging to the Pietralunga sequence (Figure 9). Map views show a NW-trending structure confined in a narrow band less than 2 km wide. In vertical cross sections, the events highlight a NE-dipping structure, whose dip is about 65° in the AT seismic model, corresponding to the seismic structure retrieved in the earthquake relocation study of Marzorati et al. [2014]. In the AT seismic model the hypocenters appear very well clustered, while they are much more dispersed in the 1D-Grad model. In this latter, the 1D geometry causes the events to spread along the horizontal direction, while the smooth, vertical velocity variation elongates the cluster along the dipping structure that extends from 2 to 6 km depth. On the contrary, the 3D-Tomo model presents a more clustered and less extended hypocenter distribution, more similar to that obtained in the AT seismic model. In these two cases, the elongated dipping structure presents a smaller extension from 3 km to 5 km depth. The smallest size (about 2 km) defined by both the 3D velocity models appears more realistic considering that the maximum magnitude involved (M_W 3.6) roughly corresponds to a subsurface rupture length smaller than 1 km [e.g., Wells and Coppersmith, 1994]. However, although the two 3D models exhibit similar seismicity patterns,

661 the coarse parameterization grid of the tomographic model does not allow the events to collapse
662 along a more focused image as that observed in the AT seismic model.

663

664 **5 Discussion and Conclusions**

665 The AT seismic model provides a new, detailed three-dimensional velocity image of an active
666 sector of the Northern Apennines. This is one of the few examples of deterministic velocity
667 models where three-dimensional velocity variations of P- and S- seismic waves are defined with
668 such a large amount of robust, multidisciplinary data. The AT seismic model is more complex
669 and detailed than previous velocity structures of the area constructed by inverting only passive
670 seismological data [Moretti et al., 2009; Carannante et al., 2013].

671 By modeling the first arrivals of P-waves travel times with an Eikonal finite difference algorithm
672 (Figure 5) we have showed that wave propagation in the crust is dominated by the velocity
673 inversion from the upper dolomites-anhydrites layer of the Triassic Evaporites to the phyllitic
674 layer of the Acoustic Basement, whose position at depth is extremely variable (from 2.0 km
675 depth beneath the S. Donato 1 well to 8-9 km depth in the eastern portion of the area). The shape
676 of the travel time wavefronts is essentially related to the complex geometries of such velocity
677 contrast, whose seismic markers are very well documented in seismic reflection profiles. These
678 propagation complexities are not present in the available seismological models that instead
679 provide simpler arrival time wavefronts. These models either contain smooth variations of
680 linearly interpolated velocities over coarse grids (1D-Grad and 3D-Tomo models) or include
681 unrealistic 1D velocity contrasts that extend horizontally for the entire region (1D-Layer model).
682 Both these features make it more difficult for such models to reproduce the finer scale wavefield.
683 Our study demonstrates that this limitation can have substantial effects in earthquake hypocenter
684 location.

685 The tested velocity models give the most similar location results in those areas where the
686 subsurface geological setting is characterized by a sub-horizontal layering, as for example along
687 the central part of Section 3 (Figure 8). On the contrary, the tested models provide extremely
688 different hypocenter solutions where the subsurface geometry is laterally less homogeneous. This
689 effect is evident by comparing the hypocenter locations obtained for the shallow seismicity (< 5

km depth) of the Città di Castello sequence (Figure 8, section 4). Indeed, in this case, we demonstrate how the 3D distribution of the lithostratigraphic units has a first order importance in controlling the earthquake locations.

For seismological studies, deterministic velocity models can be considered robust only if the consistency with independent seismological data is assessed through appropriate tests. In this work, we have verified whether the AT seismic model was able to correctly explain P- and S-wave first-arrivals observations of earthquake data recorded by a dense seismic network. In particular, we have assessed the quality of the AT seismic model by comparing the capability of such a "non-seismological" velocity model to locate hypocentral solutions with respect to the efficiency of a set of velocity models previously published [Moretti et al., 2009; Carannante et al., 2013], and constructed by inverting simultaneously P- and S-wave first-arrival times in one or three dimensions [Kissling et al., 1994] and [Thurber, 1983] respectively.

Test results have demonstrated that the AT seismic model is able to provide improved location solutions both in terms of travel time residuals and uncertainties. Mean rms computed over 3,275 hypocenters show a minimum reduction of 11% with respect to the relatively best seismological model. This result may be explained by the combination of two possible causes. The first one is that earthquakes selected in this study are different from those used to build the previous seismological models. In fact, these latter were "tailored" for a specific acquisition geometry and event distribution, and both their resolution and parameterization are consistent with a given data set. Therefore, it is not straightforward that those particular velocity models are also efficient to locate the present seismicity, even if they are well resolved for a given inversion layout. The second cause is related to the robustness of the AT seismic model that, thanks to the dense data set of seismic commercial lines and laboratory measurements, includes very detailed information on the small scale structures of the crust, at a resolution that the present seismological models have not yet reached.

Visual inspection of earthquake distributions has shown that the hypocenter locations computed in the AT seismic model are generally in agreement with the seismicity patterns defined in previous studies [Chiaraluce et al., 2007; Moretti et al., 2009; Marzorati et al., 2014]. Comparing to the main geological structures, we find that earthquakes following the Altotiberina fault geometry are confined in a volume having about 1 km of thickness (see Section 1 and 2 of Figure

8). The seismicity distribution defines an arcuate geometry for specific sectors of the ATF, starting from the intersection of the Gubbio fault at 5 km depth and toward its deeper tip. In our model the ATF related earthquakes do not follow a particular velocity contrast, with the exception of the Pietralunga area (Section 3 in Figure 8). Most of the deep seismicity is in fact located within the upper Crystalline Basement along and below the ATF trace. This may be considered as an artifact due to our chosen velocity model. Nevertheless, the relocation analysis of the 2000-2001 seismicity [Chiaraluce et al., 2007] highlighted the same feature, allowing the authors to interpret these events as seismic activity occurring within a 500-1000 m thick ATF damage zone. Previous studies, based on the interpretation of some seismic reflection profiles in the study area as well as the CROP-03 NVR profile, highlighted the likelihood of a thick damage zone of the ATF, or even extensional duplexes of the ATF plane at depth [Barchi et al., 1998b; Collettini and Barchi, 2002; Mirabella et al., 2011]. These observations well fit with a 500-1000 m thick damage zone associated to the fault as identified by our earthquake distribution.

The small seismic sequences occurring along the fault system are mainly located inside two lithostratigraphic units: the Carbonatic Multilayer and the Triassic Evaporites, while the underlying Acoustic Basement seems to represent a region of reduced activity. This feature is well shown in the example of the Pietralunga sequence (Figure 9) whose main shock occurs inside the deeper part of the Triassic Evaporitic layer, at about 5 km of depth, while the aftershocks occur within the upper part of the same lithostratigraphic unit. Marzorati et al. [2014] interpreted the relocated Pietralunga sequence by superimposing the hypocenter locations over two available geological sections, suggesting that the seismicity cutoff could be related to the Altotiberina fault activity. The image of the crustal structure depicted by the AT seismic model provides further and more quantitative details about the spatial correlation between seismicity and geological structures. In the Pietralunga area, our model indicates that the ATF plane crosses the Acoustic Basement and is located well below (about 1 km) the seismic activity. In fact, we found that the seismicity located in the AT seismic model occurs within a brittle layer corresponding to the Triassic Evaporites while the phyllitic layer of the Acoustic Basement represents the cutoff of the Pietralunga sequence. This evidence is the first direct correlation between seismicity and geological structures that suggests in the Pietralunga area a clear lithological control on the seismic activity evolution, in agreement with previous geological studies performed in the Gubbio area [Mirabella et al., 2008a]. Our results open new

perspectives for further investigations of the seismic activity along the Altotiberina fault system, with the possibility of constraining the mechanical behavior as long as the frictional properties of the lithologies involved in seismic faulting [Collettini et al., 2009; Scuderi et al., 2013].

The present study demonstrates that independent geophysical and geological information can provide reliable and high-resolution velocity models for earthquake location, with results that are comparable or even superior to those obtained with earthquake based tomographic models, especially when passive seismological data are not adequate to obtain detailed images of the subsurface. An advantage of locating earthquakes in deterministic velocity models is also the possibility to correlate the seismicity occurrence with the known geological structures. This correlation cannot be directly obtained using seismological models alone since the relationship between seismic velocities and physical properties of the rocks is not uniquely determined. Nevertheless, information from seismological data is still essential to characterize spatial and temporal variations of both P and S-wave velocities, especially at depths not attained by conventional exploration seismology. Thus, a new perspective should be the integration of geological and seismological data through the development of passive tomographic techniques that include the geological information into the inversion procedure. This would be possible by introducing parameterizations that take into account the real velocity contrasts of the subsurface, by inverting simultaneously passive and active seismological data, and including the velocity ranges related to the main lithostratigraphic bodies, as constrained by in situ and laboratory data. In this way, multidisciplinary approaches reconciling geological and seismological models could lead to a more complete understanding of the seismic activity in complex tectonic settings.

Acknowledgements

The AT seismic model presented in this study is available upon request to the authors. Waveform data of earthquakes located in this work were recorded by the Istituto Nazionale di Geofisica e Vulcanologia and are available from the European Integrated Data Archive (EIDA) at http://eida.rm.ingv.it. The NonLinLoc software package is available at http://www.alomax.net/nlloc. We thank Midland valley exploration ltd for providing the MOVE(TM) package. Figures were made using the Generic Mapping Tool software [Wessel and

780 Smith, 1998]. This work was supported by PREMIALE 2011 project: *Studio multidisciplinare*
781 *della fase di preparazione di un terremoto* (cap. 3.1.01.01; cod. team 0551.020). FT was
782 supported by "*Progetto di Ateneo 2013 Sapienza*". We are grateful to Simona Carannante,
783 Milena Moretti and coauthors for providing us the regional 1D velocity model and the 3D
784 tomographic model of the Altotiberina region. We wish to thank Andrea Lupattelli for providing
785 us important hints on the AT geological model. We thank the Associate Editor and the
786 Reviewers for their comments and suggestions which have improved this manuscript.

787

788 **References**

789 Aldersons, F. (2004), Toward a three-dimensional crustal structure of the Dead Sea region from
790 local earthquake tomography, PhD. Thesis, Tel-Aviv University, pp. 123.

791 Anelli, L., M. Gorza, M. Pieri, and M. Riva (1994), Subsurface well data in the Northern
792 Apennines (Italy), Mem. Soc. Geol. Ital. 48, 461-471.

793 Bally, A., L. Burbi,, C. Cooper, and R. Ghelardoni (1986), Balanced sections and seismic
794 reflection profiles across the central Apennines, Mem. Soc. Geol. Ital. 35, 257–310.

795 Barchi, M. (1991), Integration of a seismic profile with surface and subsurface geology in a
796 cross-section through the Umbria-Marche Apennines, Boll. Soc. Geol. Ital. 110, 469-479.

797 Barchi, M., R. Minelli, and G. Pialli (1998a), The crop 03 profile: a synthesis of results on deep
798 structures of the northern Apennines, Mem. Soc. Geol. Ital. 52, 383–400.

799 Barchi, M., A. De Feyter, M. Magnani, G. Minelli, G. Pialli, and B. Sotera (1998b), Extensional
800 tectonics in the Northern Apennines (Italy): evidence from the CROP03 deep seismic reflection
801 line, Mem. Soc. Geol. Ital. 52, 528–538.

802 Barchi, M., A. De Feyter, B. Magnani, G. Minelli, G. Pialli, and B. Sotera (1998c), The
803 structural style of the Umbria–Marche fold and thrust belt, Mem. Soc. Geol. Ital. 52, 557–578.

804 Barchi, M. (2002), Lithological and structural controls on the seismogenesis of the Umbria
805 region: observations from seismic reflection profiles, Boll. Soc. Geol. It., Vol. Spec. 1, 855-864.

806 Barchi, M. (2010), The Neogene-Quaternary evolution of the Northern Apennines: crustal
807 structure, style of deformation and seismicity, in M. Beltrando; A. Peccerillo; M. Mattei; S.
808 Conticelli & C. Doglioni, ed., 'The Geology of Italy', Journal of Virtual Explorer.

809 Batini, F., G. Bertini, G. Gianelli, and E. Pandeli (1983), Deep structure of the Larderello field:
810 Con- tribution from recent geophysical and geological data, Mem. Soc. Geol. Ital., 25, 219 –
811 235.

812 Bethoux N., T. Theunissen, M. O. Beslier, Y. Font, F. Thouvenot, J. X. Dessa, S. Simon, G.
813 Courrioux, A. Guillen (2016), Earthquake relocation using a 3D a-priori geological velocity
814 model from the western Alps to Corsica : implication for seismic hazard. Tectonophysics 670, p.
815 82-100. ISSN 0040-1951.

816 Boncio, P., F. Brozzetti, F. Ponziani, M. R. Barchi, G. Lavecchia, and G. Pialli (1998),
817 Seismicity and extensional tectonics in the northern Umbria-Marche Apennines, Mem. Soc.
818 Geol. It., 52, 539-556

819 Boncio, P., F. Brozzetti, and G. Lavecchia (2000), Architecture and seismotectonics of a regional
820 low-angle normal fault zone in central Italy, Tectonics 19, 1038–1055.

821 Bostock, M. G., and N. I. Christensen (2012), Split from slip and schist: Crustal anisotropy
822 beneath northern Cascadia from non-volcanic tremor, J. Geophys. Res., 117, B08303,
823 doi:10.1029/2011JB009095.

824 Brocher, T. M. (2005), Compressional and shear wave velocity versus depth in the San Francisco
825 Bay Area, California: rules for USGS Bay Area Velocity Model 05.0.0, U.S. Geol. Surv. Open-
826 File Rept. 2005-1317.

827 Burlini, L., and S. Tancredi (1998), Experimental study of the seismic properties of Isola d'Elba
828 metamorphic basement (Tuscany, Italy), Memorie della Società Geoligica Italiana, 52, 101–110.

829 Carannante, S., G. Monachesi, M. Cattaneo, A. Amato, and C. Chiarabba (2013), Deep structure
830 and tectonics of the northern-central Apennines as seen by regional-scale tomography and 3-D
831 located earthquakes, J. Geophys. Res., 118, 5391–5403, doi:10.1002/jgrb.50371.

832 Carminati E., L. Corda, G. Mariotti, A. Scion, and F. Trippetta (2013), Mesozoic Syn- and

833 Postrifting Evolution of the Central Apennines, Italy: The Role of Triassic Evaporites, The
834 Journal of Geology, 121, 4, pp. 327-354.

835 Chiarabba, C., S. Bagh, I. Bianchi, P. De Gori, and M. Barchi (2010), Deep structural
836 heterogeneities and the tectonic evolution of the Abruzzi region (Central Apennines, Italy)
837 revealed by microseismicity, seismic tomography, and teleseismic receiver functions, Earth
838 Planet. Sci. Lett. 295, 462-476.

839 Chiaraluce, L., C. Chiarabba, C. Collettini, D. Piccinini, M. Cocco (2007), Architecture and
840 mechanics of an active low angle normal fault: Alto Tiberina Fault, Northern Apennines, Italy, J.
841 Geophys. Res. 112, B10310. http://dx.doi.org/10.1029/2007JB005015.

842 Chiaraluce, L., et al. (2014), The Alto Tiberina Near Fault Observatory (northern Apennines,
843 Italy), Ann. Geophys., 57, S0327, doi:10.4401/ag-6426.

844 Collettini, C., M. Barchi, C. Pauselli, C. Federico, and G. Pialli (2000), Seismic expression of
845 active extensional faults in northern Umbria (central Italy), J. Geodyn., 29, 309–321,
846 doi:10.1016/S0264-3707(99)00059-9.

847 Collettini, C., and M. R. Barchi (2002), A low angle normal fault in the Umbria region (central
848 Italy): A mechanical model for the related microseismicity, Tectonophysics, 359, 97–115.

849 Collettini, C., Chiaraluce, L., Pucci, S., Barchi, M.R., Cocco, M. (2005), Looking at fault
850 reactivation matching structural geology and seismology, J. Struct. Geol. 5, 937–942.

851 Collettini, C., De Paola, N., and Faulkner, D.R. (2009), Insights on the geometry and mechanics
852 of the Umbria-Marche earthquakes (Central Italy) from the integration of field and laboratory
853 data. Tectonophysics, 476(1-2), 99-109, doi:10.1016/j.tecto.2008.08.013.

854 Cushing, E. M., O. Bellier, S. Nechtschein, M. Sebrier, A. Lomax, Ph. Volant, P. Dervin, P.
855 Guignard, and L. Bove (2008), A multidisciplinary study of a slow-slipping fault for seismic
856 hazard assessment: the example of the Middle Durance Fault (SE France). Geophys. J. Int., 172,
857 1163–1178, doi: 10.1111/j.1365-246X.2007.03683.x

858 De Franco, R., R. F. Ponziani, G. Biella, G. Boniolo, G. Caielli,, A. Corsi,, M. Maistrello, and A.
859 Morrone (1998), Dss-war experiment in support of the Crop03 project, Mem. Soc. Geol. Ital., V.
860 52, pp. 67-90.

861 Di Stefano, R., F. Aldersons, E. Kissling, P. Baccheschi, C. Chiarabba, and D. Giardini (2006),
862 Automatic seismic phase picking and consistent observation error assessment: application to the
863 Italian seismicity, Geophys. J. Int., 165, 121-134.

864 Di Stefano, R., C. Chiarabba, L. Chiaraluce, M. Cocco, P. De Gori, D. Piccinini, and L. Valoroso
865 (2011), Fault zone properties affecting the rupture evolution of the 2009 (Mw 6.1) L'Aquila
866 earthquake (central Italy): Insights from seismic tomography, Geophys. Res. Lett., 38,
867 doi:10.1029/2011GL047365.

868 Di Stefano R., L. Chiaraluce, L. Valoroso, F. Waldhauser, D. Latorre, D. Piccinini, and E. Tinti
869 (2014), An automatic modular procedure to generate high-resolution earthquake catalogues:
870 application to the Alto Tiberina Near Fault Observatory (TABOO), Italy, AGU Fall Meeting,
871 Dicembre 2014.

872 Elter, P., G. Giglia, M. Tongiorgi, and L. Trevisan (1975), Tensional and compressional areas in
873 the recent (Tortonian to Present) evolution of north Apennines, Bollettino di Geofisica
874 TeoricaedApplicata 17, 3-18.

875 Font, Y., H. Kao, S. Lallemand, C.-S. Liu, and L.-Y. Chiao (2004). Hypocentral determination
876 offshore Eastern Taiwan using the Maximum Intersection method, Geophys. J. Int. 158, 655–
877 675.

878 Ghelardoni, R. (1962), Stratigrafia e tettonica del Trias di M.Malbe presso Perugia, Boll. Soc.
879 Geol. Ital., 81, 66 – 75.

880 Gibbons, J. D., and S. Chakraborti (2011), Nonparametric Statistical Inference, 5th Ed., Boca
881 Raton, FL: Chapman & Hall/CRC Press, Taylor & Francis Group

882 Husen, S, E. Kissling, N. Deichmann, S. Wiemer, D. Giardini, and M. Baer (2003), Probabilistic
883 earthquake location in complex three-dimensional velocity models: Application to Switzerland, J
884 Geophys Res 108:2077–2102.

885 Husen, S, and R. B. Smith (2004), Probabilistic Earthquake Relocation in Three-Dimensional
886 Velocity Models for the Yellowstone National Park Region, Wyoming, Bull Seism Soc Am
887 94:880–896.

888 Husen, S., and J. L. Hardebeck (2010), Earthquake location accuracy, Community Online
889 Resource for Statistical seismicity Analysis, doi:10.5078/corssa-55815573.

890 Jaeger, J. C., N. G. W. Cook, and R. W. Zimmerman (2007), Fundamentals of Rock Mechanics,
891 Fourth Edition, Blackwell Publishing, p. 475.

892 Keller, J., G. Minelli, and G. Pialli (1994), Anatomy of a late orogenic extension: the Northern
893 Apeninnes case, Tectonophysics 238, 275-294.

894 Kim, W., I.-K. Hahm, S. J. Ahn, and D. H. Lim (2006), Determining the hypocentral parameters
895 for local earthquakes in 1-D using genetic algorithms, J. Geophys. Int. 166, 590-600.

896 Kissling E., W. L. Ellsworth, D. Eberhart-Phillips, and U. Kradolfer (1994), Initial reference
897 models in local earthquake tomography, J. Geophys. Res. 99, 19,635-19,646.

898 Korger, E. I. M., and V. Schlindwein (2012), Performance of localization algorithms for
899 teleseismic mid-ocean ridge earthquakes: the 1999 Gakkel Ridge earthquake swarm and its
900 geological interpretation, Geophys. J. Int. 188, 613–625.

901 Lomax, A., J. Virieux, P. Volant, and C. Berge (2000), Probabilistic earthquake location in 3D
902 and layered models: introduction of a Metropolis-Gibbs method and comparison with linear
903 locations, in Advances in Seismic Event Location, C. H. Thurber and N. Rabinowitz (Editors),
904 Kluwer, Amsterdam, 101–134.

905 Lomax, A. A. Zollo, P. Capuano, and J. Virieux (2001), Precise, absolute earthquake location
906 under Somma-Vesuvious volcano using a new 3D velocity model, Geophys. J. Int. 146, 313-331.

907 Lomax, A. (2005), A reanalysis of the hypocentral location and related observations for the great
908 1906 California earthquake, Bull. Seism. Soc. Am., 95, 861-877, doi:10.1785/0120040141.

909 Lomax, A. (2008), Location of the Focus and Tectonics of the Focal Region of the California
910 Earthquake of 18 April 1906, Bull. Seism. Soc. Am., 98, 846–860, doi: 10.1785/0120060405

911 Lomax, A., A. Michelini, and A. Curtis (2009), Earthquake Location, Direct, Global-Search
912 Methods, in Encyclopedia of Complexity and System Science, Part 5, Meyers, R. A. (ed.),
913 Springer, New York, 2449-2473, doi:10.1007/978-0-387-30440-3.

914 Mallet, J.L. (1989), Discrete Smooth Interpolation, ACM-Transictions on Graphics, 8, 121-144.

915 Mallet, J.L. (1992), gOcad: A Computer-Aided Design Program for Geological Application, in
916 Turner, K. (ed.), Three-Dimensional Modeling with Geoscientific Information Systems, Kluwer
917 Academic Publishers, Dordrecht, Holland, Nato ASI Series C, V. 354, 123-141.

918 Martinis, B., and M. Pieri (1964), Alcune notizie sulla formazione evaporitica del Triassico
919 superiore nell'Italia centrale e meridionale, Memorie della Società Geoligica Italiana 4, 649–678.

920 Marzorati S., M. Massa, M. Cattaneo, G. Monachesi, and M. Frapiccini (2014), Very detailed
921 seismic pattern and migration inferred from the April 2010 Pietralunga (northern Italian
922 Apennines) micro-earthquake sequence, Tectonophysics 91-109,
923 doi:10.1016/j.tecto.2013.10.014.

924 Miller S. L. M. and R. R. Stewart (1990), Effect of lithology, porosity and shaliness on P- and
925 S.wave velocities from sonic logs, Can. J. of Expl. Geophys., 26, 94-103.

926 Mirabella, F., M. Ciaccio, M. Barchi, and S. Merlini (2004), The Gubbio normal fault (central
927 Italy): Geometry, displacement distribution and tectonic evolution, J. Struct. Geol., 26, 2233–
928 2249, doi:10.1016/j.jsg.2004.06.009.

929 Mirabella, F., M. Barchi, A.Lupattelli, E.Stucchi, and M.Ciaccio (2008a), Insights on the
930 seismogenic layer thickness from the upper crust structure of the Umbria-Marche Apennines
931 (central Italy). Tectonics 27, TC1010. http://dx.doi.org/10.1029/2007TC002134.

932 Mirabella, F., M. Barchi, and A. Lupattelli (2008b), Seismic reflection data in the Umbria-
933 Marche region: Limits and capabilities to unravel the sub-surface structure in a seismically active
934 area, Ann. Geophys., 51(2/3), 383–396.

935 Mirabella, F., F. Brozzetti, A.Lupattelli, and M.R. Barchi (2011), Tectonic evolution of a low-
936 angle extensional fault system from restored cross-sections in the Northern Apennines (Italy).
937 Tectonics 30, TC6002. http://dx.doi.org/10.1029/2011TC002890.

938 Moretti, M., P. De Gori, and C. Chiarabba (2009), Earthquake relocation and three-dimensional
939 Vp and Vp/Vs model along the low angle Alto tiberina Fault (central Italy): evidence for fluid
940 overpressure, Geophys. J. Int., 176(3), 833-846, doi:10,1111/j.1365-246X.2008.03984.x.

941 Moser, T.J., T. van Eck, and G. Nolet (1992), Hypocenter determination in strongly
942 heterogeneous earth models using the shortest path method, J. Geophys. Res., 97, 6563-6572.

943 Patacca, E., and P. Scandone (2001), Late thrust propagation and sedimentary response in the
944 thrust-belt foredeep system of the southern Apennines (Pliocene-Pleistocene), in Anatomy of an
945 Orogen: The Apennines and Adjacent Mediterranean Basins, edited by G. Vai and I. Martini, pp.
946 441 – 454, Kluwer Acad., Norwell, Mass.

947 Pauselli, C., R. Marchesi, and M. Barchi (2002), Seismic image of the compressional and
948 extensional structures in the Gubbio area (Umbrian-Pre Apennines), Boll. Soc. Geol. Ital., Vol.
949 Spec. 1, 263 – 272.

950 Pialli, G., M. Barchi, and G. Minelli (1998), Results of the CROP03 deep seismic reflection
951 profile, Mem. 52., 657 pp., Soc. Geol. Ital., Rome.

952 Piccinini, D., M. Cattaneo, C. Chiarabba, L. Chiaraluce, M. De Martin, M. Di Bona, M. Moretti,
953 G. Selvaggi, P. Augliera, D. Spallarossa, G. Ferretti, A. Michelini, A. Govoni, P. Di Bartolomeo,
954 M. Romanelli, and J. Fabbri (2003), A microseismic study in a low seismicity area of Italy: the
955 Città di Castello 2000-2001 experiment, Annals of Geophysics, 46 (6), 1315-1324.

956 Podvin, P. and I. Lecomte (1991), Finite difference computation of traveltimes in very contrasted
957 velocity models: a massively parallel approach and its associated tools.,Geophys. J. Int., 105,
958 271-284.

959 Ponziani, F., R. De Franco, G. Minelli, G. Biella, C. Federico, and G. Pialli (1995), Crustal
960 shortening and duplication of the Moho in the northern Apennines: A view from seismic
961 refraction data, Tectonophysics, 252, 391-418.

962 Pucci, S., F. Mirabella, F. Pazzaglia, M. Barchi, L. Melelli, P. Tuccimei, M. Soligo, and L.
963 Saccucci (2014), Interaction between regional and local tectonic forcing along a complex

964 Quaternary extensional basin: Upper Tiber Valley, Northern Apennines, Italy. Quaternary
965 Science Reviews 102, 111-132.

966 Scarsella, F. (1951), Un aggruppamento di pieghe dell' AppenninoUmbro-
967 Marchigiano.Bollettino del ServizioGeologicod'Italia 73, 309-320.

968 Scuderi, M. M., Niemeijer, A.R., Collettini, C. and Marone C. (2013), Frictional properties and
969 slip stability of active faults within carbonate-evaporite sequences: The role of dolomite and
970 anhydrite. Earth and Planet. Sci. Lett., 369, 220-232, doi:10.1016/j.epsl.2013.03.024.

971 Smeraglia, L., F. Trippetta, E. Carminati, and S. Mollo (2014), Tectonic control on the
972 petrophysical properties of foredeep sandstones in the Central Apennines, Italy, J. Geophys.
973 Res., 119, 9077-9094, doi:10.1002/2014JB011221.

974 Smith, S. A. F., C. Collettini, and R. E. Holdworth (2008), Recognizing the seismic cycle along
975 ancient faults: CO2-induced fluidization of breccias in the footwall of a sealing low-angle
976 normal fault, J. Struct. Geol., 30, 1034-1046, doi:10.1016/j.jsg.2008.04.010

977 Tarantola, A. and B. Valette (1982), Inverse problems = quest for information., Journal of
978 Geophysics, 50, 159-170.

979 Thurber, C. H. (1983), Earthquake locations and three-dimensional crustal structure in the coyote
980 lake area, Central California, J. Geophys. Res., 88 (B10), 8226–8236,
981 doi:10.1029/JB088iB10p08226.

982 Trippetta, F., C. Collettini, S. Vinciguerra, and P. G. Meredith (2010), Laboratory measurements
983 of the physical properties of Triassic Evaporites from Central Italy and correlation with
984 geophysical data. Tectonophysics 492, 121–132. http://dx.doi.org/10.1016/j.tecto.2010.06.001.

985 Trippetta, F., C. Collettini, M.R. Barchi, A. Lupattelli, and F. Mirabella (2013a), A
986 multidisciplinary study of a natural example of a CO 2 geological reservoir in central Italy, Int. J.
987 Greenhouse Gas Control 12, 72–83. http://dx.doi.org/10.1016/j.ijggc.2012.11.010.

988 Trippetta F, C. Collettini, P.G. Meredith, and S. Vinciguerra (2013b), Evolution of the elastic
989 moduli of seismogenic Triassic Evaporites subjected to cyclic stressing. Tectonophysics,
990 592:67–79.

991 Trippetta F., M.M. Scuderi, and C. Collettini (2015), Physical and Transport Properties of the
992 carbonate-bearing faults: experimental insights from the Monte Maggio Fault zone (Central
993 Italy). EGU General Assembly Conference Abstracts 17, 11532.

994 Wagner, M., S. Husen, A. Lomax, E. Kissling, and D. Giardini (2013), High-precision
995 earthquake locations in Switzerland using regional secondary arrivals in a 3D velocity model,
996 Geophys. J. Int., 193, 1589-1607, doi: 10.1093/gji/ggt052.

997 Wang, X.-Q., A. Schubnel, J. Fortin, E. C. David, Y. Gueguen, and H.-K. Ge (2012), High
998 Vp/Vs ratio: Saturated cracks or anisotropy effects?, Geophys. Res. Lett., 39, L11307,
999 doi:10.1029/2012GL051742.

1000 Wells, D.L., and K.J. Coppersmith (1994), New empirical relationships among magnitude,
1001 rupture length, rupture width, rupture area, and surface displacement: Bulletin of the
1002 Seismological Society of America, v. 84, p. 974-1002.

1003

1004 **Captions**

1005 Table 1. Seismostratigraphic units and seismic velocities associated to the five lithological
1006 groups of the AT seismic model. P-wave velocities used to convert in depth the seismic horizons
1007 are shown in column 2. Average P-wave velocities and Vp/Vs ratio defined in this study from in
1008 situ and laboratory measurements are reported in columns 3 and 4.

1009 Figure 1. (a) Geological sketch of the Upper Tiber Valley. The legend describes the main
1010 lithostratigraphic units outcropping in the area and symbols used in the map. The white box
1011 delimits the area covered by the Altotiberina seismic model. (b) Geological cross section along
1012 the S3 profile [Mirabella et al., 2011] whose position is plotted in map. (c) Location map of the
1013 seismic reflection profiles (black lines) recorded by the ENI oil Enterprise. The blue lines are the
1014 profiles of the time-migrated seismic sections presented in Figure 3a. Red line indicates the
1015 position of the seismic reflection profile recorded in the framework of the CROP-03 project.
1016 Yellow diamonds represent the location of the deep wells drilled by the ENI Enterprise oil. (d)
1017 Time-migrated seismic sections recorded beneath the S. Donato 1 (left) and the M. Civitello 1
1018 (right) wells; two stratigraphic sketches of the wells are displayed near the two sections: some

reflective horizons are correlated with either the top of the stratigraphic units or the main geological markers (i.e., Marne a Fucoidi, MF). Color codes are detailed in the legend. All the figures are modified from Mirabella et al. [2011].

Figure 2. Comparison between P-wave velocities and Vp/Vs ratio from laboratory (grey scale), P-wave velocities from boreholes (green line), and velocity values suggested by the integration of in situ and laboratory measurements (red line). (a) Schematic stratigraphic log of the Umbria Marche formations. (b) Comparison between synthetic P-wave velocity-depth profile calculated from the laboratory, P-wave velocity range measurements for each seismostratigraphic unit (see the text for referring data) and in situ P-wave velocity measurements from the Monte Civitello sonic log (green line). (c) V_P/V_S ratio range at increasing depth calculated for each seismostratigraphic unit from laboratory data (see text for detailed explanation).

Figure 3. (a) Time-migrated seismic images located along the S3 profile and their interpretation proposed by Mirabella et al. [2011]. The position on map of the interpreted seismic lines and the S3 profile are indicated in Figures 1c and 1a, respectively. (b) Vertical cross-section of the Altotiberina geological model along the S3 profile, modified from Mirabella et al. [2011]. (c) Vertical cross-section of the depth converted seismic horizons. (d) Vertical cross-section of the AT seismic model along the same trace of (b) and (c). P-wave velocities and Vp/Vs values adopted for this model are indicated in columns 2 and 4 of Table 1. Black isolines indicate the interpolated contours of P-wave travel-time wavefronts (in seconds) computed with the Eikonal finite-difference scheme of Podvin and Lecomte [1991] for an earthquake hypocenter (yellow star) located along the Altotiberina fault. The position of the S. Donato 1 and M. Civitello 1 wells is projected on the cross section.

Figure 4. (a) Map of the study area and acquisition geometry: permanent and temporary seismic stations are represented with red and green inverted triangles, respectively. Dark and light gray dots are the preliminary hypocenter locations of the two selected data sets computed in the 1D velocity model of Carannante et al. [2013] (see the text for further details); blue diamonds indicate the position of San Donato well (SD), Monte Civitello 1 well (MC), Perugia 1 well (P), Burano well (B) and Pieve di Santo Stefano well (ST). The three "beach balls" show the Time Domain Moment Tensor (TDMT) focal mechanism solutions of the Mw 3.6 Pietralunga earthquake (04/15/2010), the Mw 3.6 Città di Castello earthquake (05/08/2013) and the Mw 3.9

Gubbio earthquake (12/22/2013) (http://cnt.rm.ingv.it/tdmt). Brown lines indicate the breakaway portion of the Altotiberina fault and the Gubbio fault retrieved by Mirabella et al. [2004, 2011]. (b) Vertical cross section showing the projection of the earthquake hypocenters located in a 10 km wide area around the A-B profile.

Figure 5. Vertical cross-sections along the SW-NE oriented S3 profile of the velocity models analyzed in the present work (see Figure 1a for its position on map): (a) the AT seismic model, (b) the 3D-Tomo model from Moretti et al. [2009], (c) the 1D-Layer model from Moretti et al [2009], and (d) the 1D-Grad model from Carannante et al [2013]. Red star represents a hypothetical earthquake located along the Altotiberina fault (red line) and used to compute the travel time wavefronts (black isolines) in the four models. Isolines are drawn at regular time intervals (thin lines every 0.25 s and thick black lines every 1 s).

Figure 6. Maximum likelihood location solutions computed for 3,275 selected events in the AT seismic model, compared with the solutions obtained for the three tested velocity models: the 3D-Tomo model of Moretti et al. [2009], the 1D-Layer model of Moretti et al. [2009], and the 1D-Grad model of Carannante et al. [2013] (panels a, b and c, respectively). Left column (a1, b1 and c1): each dot indicates an earthquake location solution, whose coordinates are the rms (root-mean-squares of weighted travel time residuals) obtained for the analyzed velocity models. The horizontal axis represents the rms estimated in the AT-seismic model, the vertical axis indicates the rms computed in the 3D-Tomo model (a1), in the 1D-Layer model (b1), and in the 1D-Grad model (c1). Histograms a2, b2 and c2, show the rms distribution of the located earthquakes in the AT-seismic model (blue bins) and the tested velocity models (red bins). The two histograms to the right display the distribution the P-wave residual times (a3, b3, and c3) and the S-wave residual times (a4, b4, and c4). The mean value and the standard deviation (std) of each distribution are reported in each panel, as well as the mean rms reduction of earthquakes located in the AT-seismic model with respect to the other velocity models.

Figure 7. Distribution of the uncertainty estimators computed in the AT seismic model (red bins) and compared with the solutions (blue bins) obtained in the 3D-Tomo model (panel a), the 1D-Layer model (panel b), and the 1D-Grad model (panel c). From left to right, plots show the distribution of the PDF volume, the distance of the maximum likelihood hypocenter location from the expectation location, the 68% spatial error along the horizontal direction, and the 68%

spatial error along the vertical direction. These errors are computed only for selected events whose distance between the maximum likelihood location and the expectation location is lower than 0.5 km. For each histogram we report the median value and the median reduction computed comparing the results of the AT seismic model with respect to the other velocity models.

Figure 8. Vertical cross sections of the tested velocity models along four SW-NE profiles. From top to bottom: the AT seismic model, the 3D-Tomo model of Moretti et al. [2009], the 1D-Layer model of Moretti et al. [2009], and the 1D-Grad model of Carannante et al. [2013]. Black dots indicate the projection of the maximum likelihood hypocenter locations computed in each model and confined in a ± 1 km wide zone around the cross-sections, except Section 1 where the projection zone is ± 2.5 km wide. The yellow star is the hypocenter of the Mw 3.9 Gubbio earthquake (12/22/2013) located in the AT seismic model. Red lines represent the trace of the Altotiberina low-angle normal fault and the Gubbio high-angle normal fault from Mirabella et al. [2004b; 2011]. Red dashed line marks the zone of microseismicity around Altotiberina fault as deduced in this work. Velocity color code is the same for all the models. Velocity-unit correlation of the AT seismic model is indicated in the color scale at the bottom of the figure.

Figure 9. Spatial distribution of the seismicity (613 maximum likelihood hypocenters) recorded during the April 2010 Pietralunga Sequence and located in the three velocity models. From top to bottom: the AT seismic model, the 3D-Tomo model of Moretti et al. [2009], and the 1D-Grad model of Carannante et al. [2013]. Map views show the horizontal projection of the hypocenter solutions (black dots), the closest stations to the sequence (red inverted triangles) and the traces of the three vertical cross sections displayed on the left side of the figure. Yellow star represents the hypocenter location (on map and along the cross sections) of the Mw 3.6 Pietralunga earthquake (04/15/2010) located in the AT seismic model; the beach ball is the TDMT focal mechanism solution provided by INGV (http://cnt.rm.ingv.it/tdmt). Scale color is the same than Figure 8. In the cross sections, the main seismicity alignment identified in this study is highlighted with dashed red lines.

Figure 1. Figure

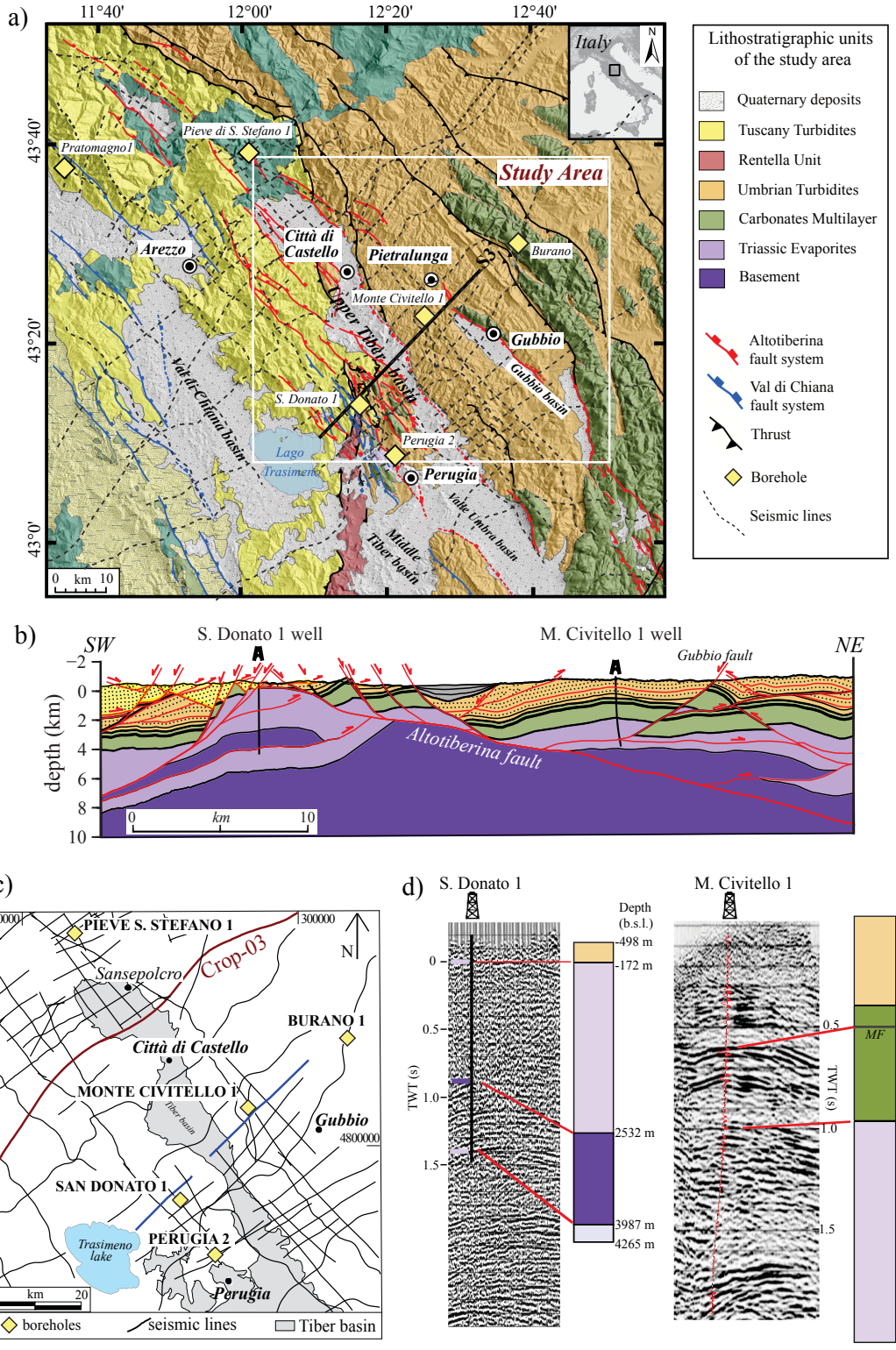
a)
11°40'
12°00'
12°20'
12°40'
43°40'
43°20'
43°0'
Italy
N
Study Area
Pieve di S. Stefano 1
Pratomagno1
Città di Castello
Arezzo
Pietralunga
Burano
Monte Civitello 1
Gubbio
Upper Tiber basin
Gubbio basin
Val di Chiana basin
S. Donato 1
Perugia 2
Lago Trasimeno
Perugia
Valle Umbra basin
Middle Tiber basin
0 km 10
Lithostratigraphic units of the study area
Quaternary deposits
Tuscany Turbidites
Rentella Unit
Umbrian Turbidites
Carbonates Multilayer
Triassic Evaporites
Basement
Altotiberina fault system
Val di Chiana fault system
Thrust
Borehole
Seismic lines
b)
SW
NE
S. Donato 1 well
M. Civitello 1 well
Gubbio fault
Altotiberina fault
depth (km)
0 km 10
c)
250000
300000
N
PIEVE S. STEFANO 1
Sansepolcro
Crop-03
BURANO 1
Città di Castello
MONTE CIVITELLO 1
Gubbio
4800000
SAN DONATO 1
PERUGIA 2
Trasimeno lake
Perugia
Tiber basin
0 km 20
boreholes
seismic lines
Tiber basin
d)
S. Donato 1
M. Civitello 1
Depth (b.s.l.)
TWT (s)
-498 m
-172 m
2532 m
3987 m
4265 m
-670 m
469 m
766 m
MF
2017 m
4930 m

Figure 2. Figure

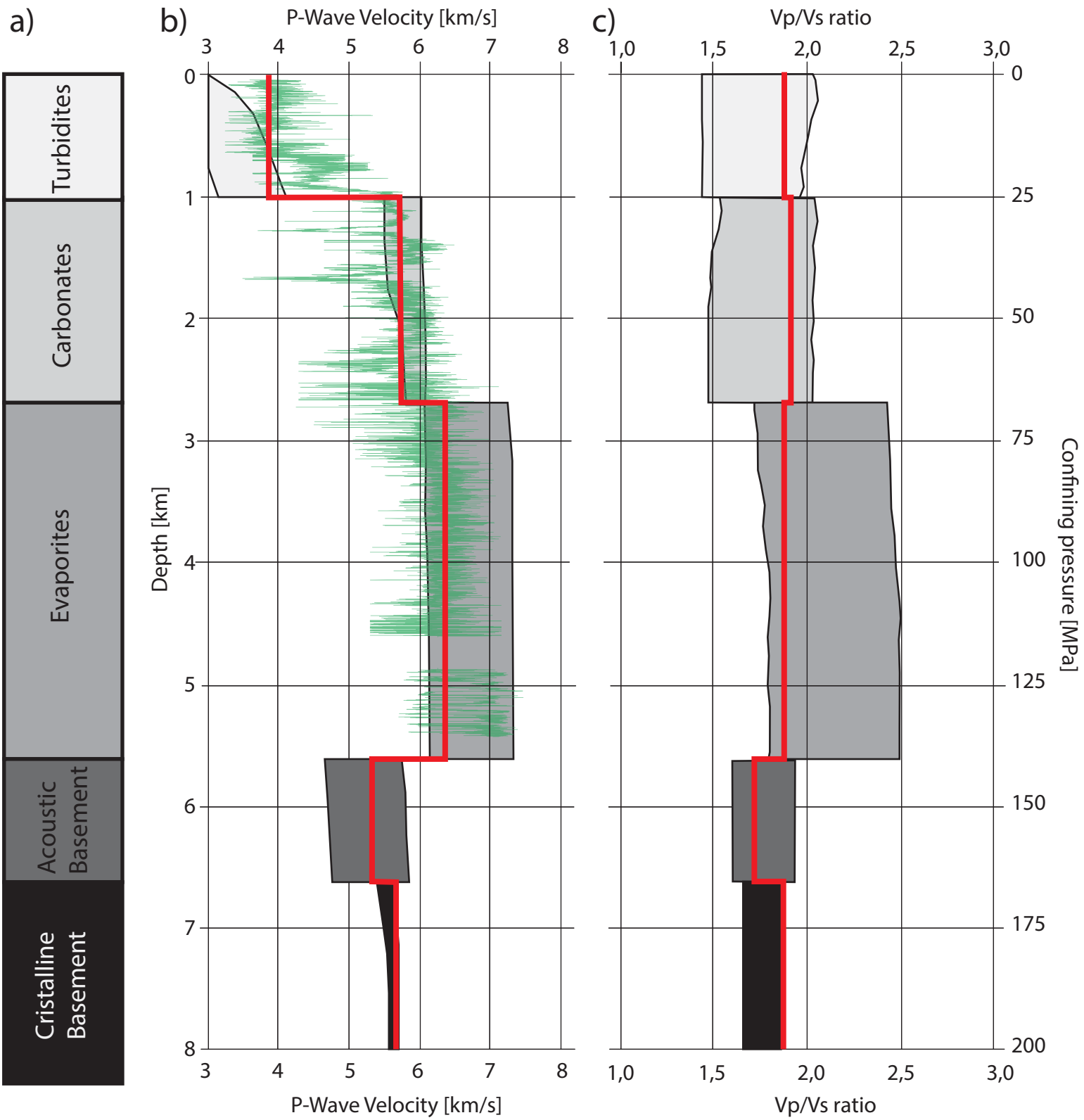
a)
Turbidites
Carbonates
Evaporites
Acoustic Basement
Cristalline Basement
b)
P-Wave Velocity [km/s]
3
4
5
6
7
8
Depth [km]
0
1
2
3
4
5
6
7
8
P-Wave Velocity [km/s]
c)
Vp/Vs ratio
1,0
1,5
2,0
2,5
3,0
Confining pressure [MPa]
0
25
50
75
100
125
150
175
200
Vp/Vs ratio

Figure 3. Figure

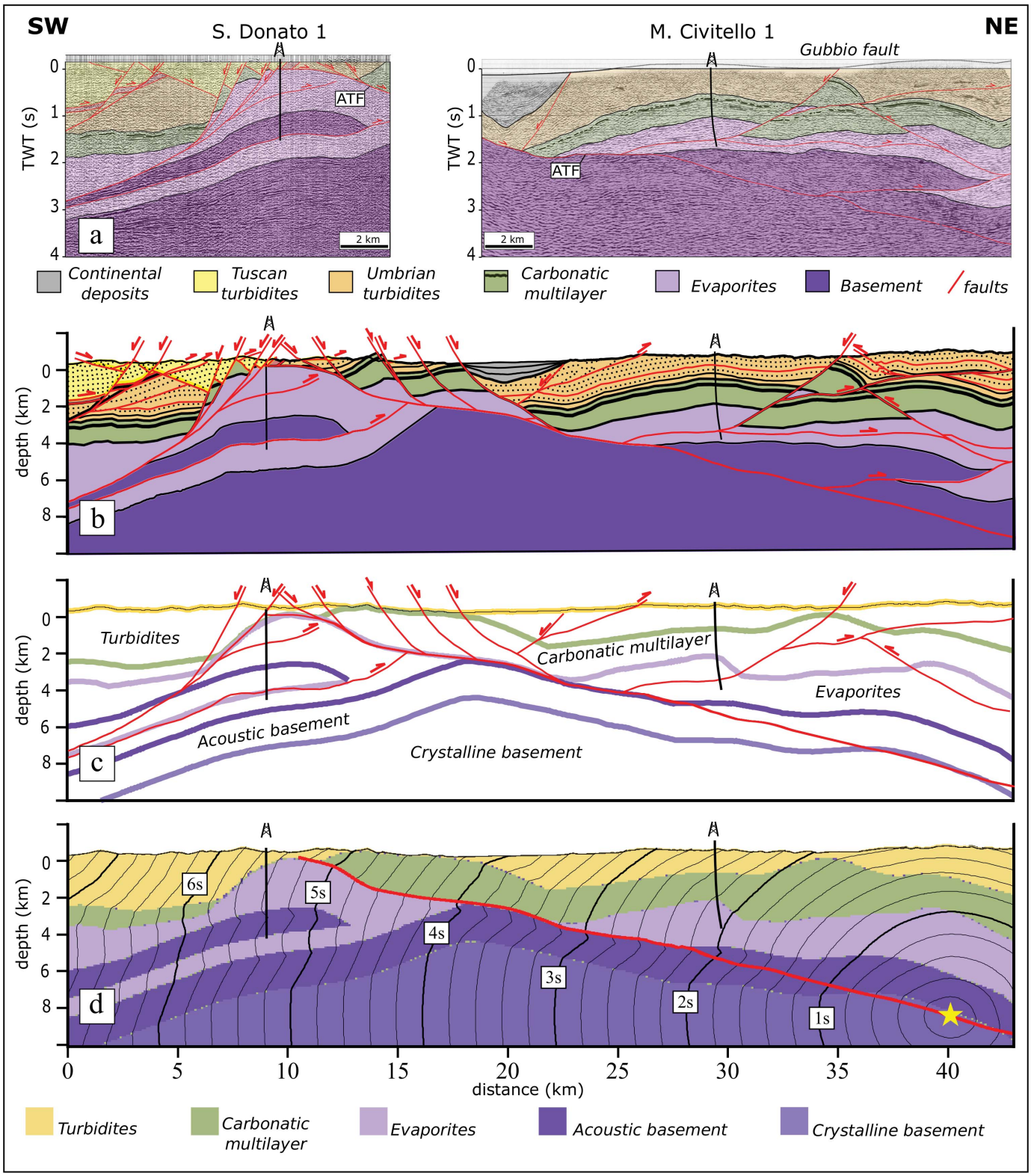
SW
NE
S. Donato 1
M. Civitello 1
Gubbio fault
ATF
TWT (s)
2 km
a
Continental deposits
Tuscan turbidites
Umbrian turbidites
Carbonatic multilayer
Evaporites
Basement
faults
depth (km)
b
Turbidites
Carbonatic multilayer
Evaporites
Acoustic basement
Crystalline basement
c
6s
5s
4s
3s
2s
1s
d
distance (km)
Turbidites
Carbonatic multilayer
Evaporites
Acoustic basement
Crystalline basement

Figure 4. Figure

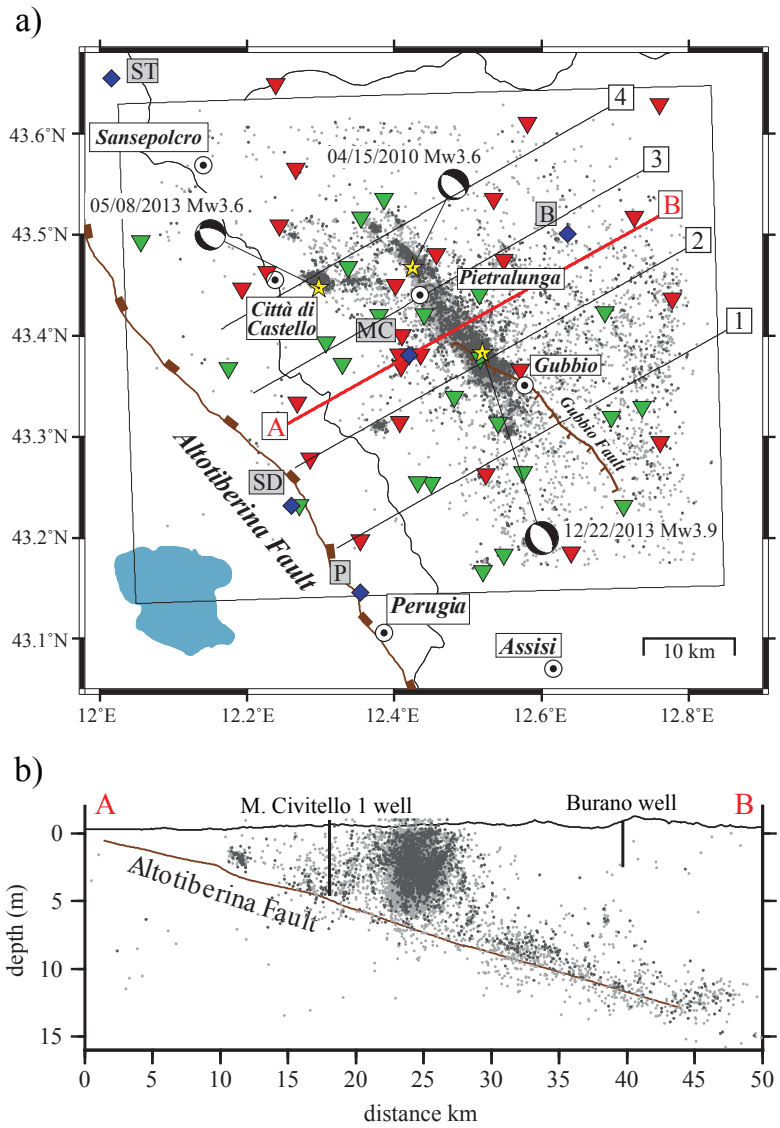
a)
ST
Sansepolcro
04/15/2010 Mw3.6
05/08/2013 Mw3.6
4
3
2
1
B
B
A
Pietralunga
Città di Castello
MC
Gubbio
Gubbio Fault
Altotiberina Fault
SD
P
12/22/2013 Mw3.9
Perugia
Assisi
10 km
43.6°N
43.5°N
43.4°N
43.3°N
43.2°N
43.1°N
12°E
12.2°E
12.4°E
12.6°E
12.8°E
b)
A
M. Civitello 1 well
Burano well
B
Altotiberina Fault
depth (m)
0
5
10
15
0
5
10
15
20
25
30
35
40
45
50
distance km

Figure 5. Figure

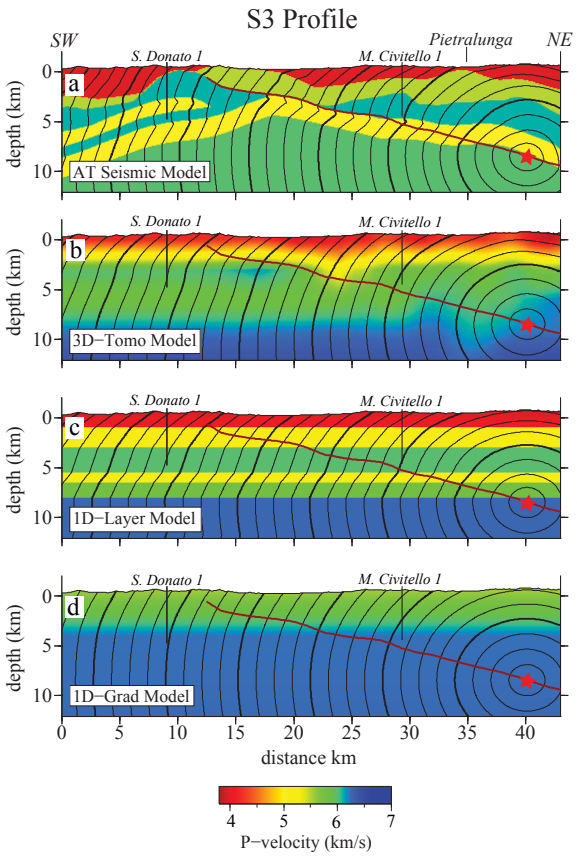
S3 Profile
SW
NE
Pietralunga
S. Donato 1
M. Civitello 1
a
AT Seismic Model
b
3D−Tomo Model
c
1D−Layer Model
d
1D−Grad Model
depth (km)
0
5
10
0 5 10 15 20 25 30 35 40
distance km
4 5 6 7
P−velocity (km/s)

Figure 6. Figure

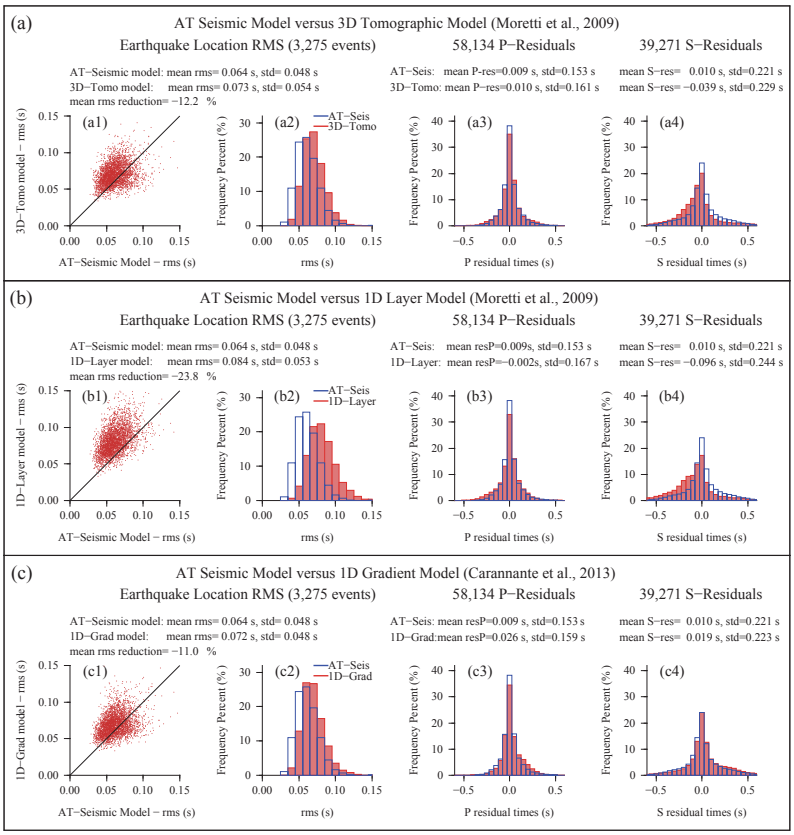
(a)
AT Seismic Model versus 3D Tomographic Model (Moretti et al., 2009)
Earthquake Location RMS (3,275 events)
58,134 P−Residuals
39,271 S−Residuals
AT−Seismic model: mean rms= 0.064 s, std= 0.048 s
3D−Tomo model: mean rms= 0.073 s, std= 0.054 s
mean rms reduction= −12.2 %
AT−Seis: mean P-res=0.009 s, std=0.153 s
3D−Tomo: mean P−res=0.010 s, std=0.161 s
mean S−res= 0.010 s, std=0.221 s
mean S−res= −0.039 s, std=0.229 s
(a1)
(a2)
(a3)
(a4)
AT−Seis
3D−Tomo
3D−Tomo model − rms (s)
AT−Seismic Model − rms (s)
Frequency Percent (%)
rms (s)
P residual times (s)
S residual times (s)
(b)
AT Seismic Model versus 1D Layer Model (Moretti et al., 2009)
Earthquake Location RMS (3,275 events)
58,134 P−Residuals
39,271 S−Residuals
AT−Seismic model: mean rms= 0.064 s, std= 0.048 s
1D−Layer model: mean rms= 0.084 s, std= 0.053 s
mean rms reduction= −23.8 %
AT−Seis: mean resP=0.009s, std=0.153 s
1D−Layer: mean resP=−0.002s, std=0.167 s
mean S−res= 0.010 s, std=0.221 s
mean S−res= −0.096 s, std=0.244 s
(b1)
(b2)
(b3)
(b4)
AT−Seis
1D−Layer
1D−Layer model − rms (s)
AT−Seismic Model − rms (s)
Frequency Percent (%)
rms (s)
P residual times (s)
S residual times (s)
(c)
AT Seismic Model versus 1D Gradient Model (Carannante et al., 2013)
Earthquake Location RMS (3,275 events)
58,134 P−Residuals
39,271 S−Residuals
AT−Seismic model: mean rms= 0.064 s, std= 0.048 s
1D−Grad model: mean rms= 0.072 s, std= 0.048 s
mean rms reduction= −11.0 %
AT−Seis: mean resP=0.009 s, std=0.153 s
1D−Grad:mean resP=0.026 s, std=0.159 s
mean S−res= 0.010 s, std=0.221 s
mean S−res= 0.019 s, std=0.223 s
(c1)
(c2)
(c3)
(c4)
AT−Seis
1D−Grad
1D−Grad model − rms (s)
AT−Seismic Model − rms (s)
Frequency Percent (%)
rms (s)
P residual times (s)
S residual times (s)

Figure 7. Figure

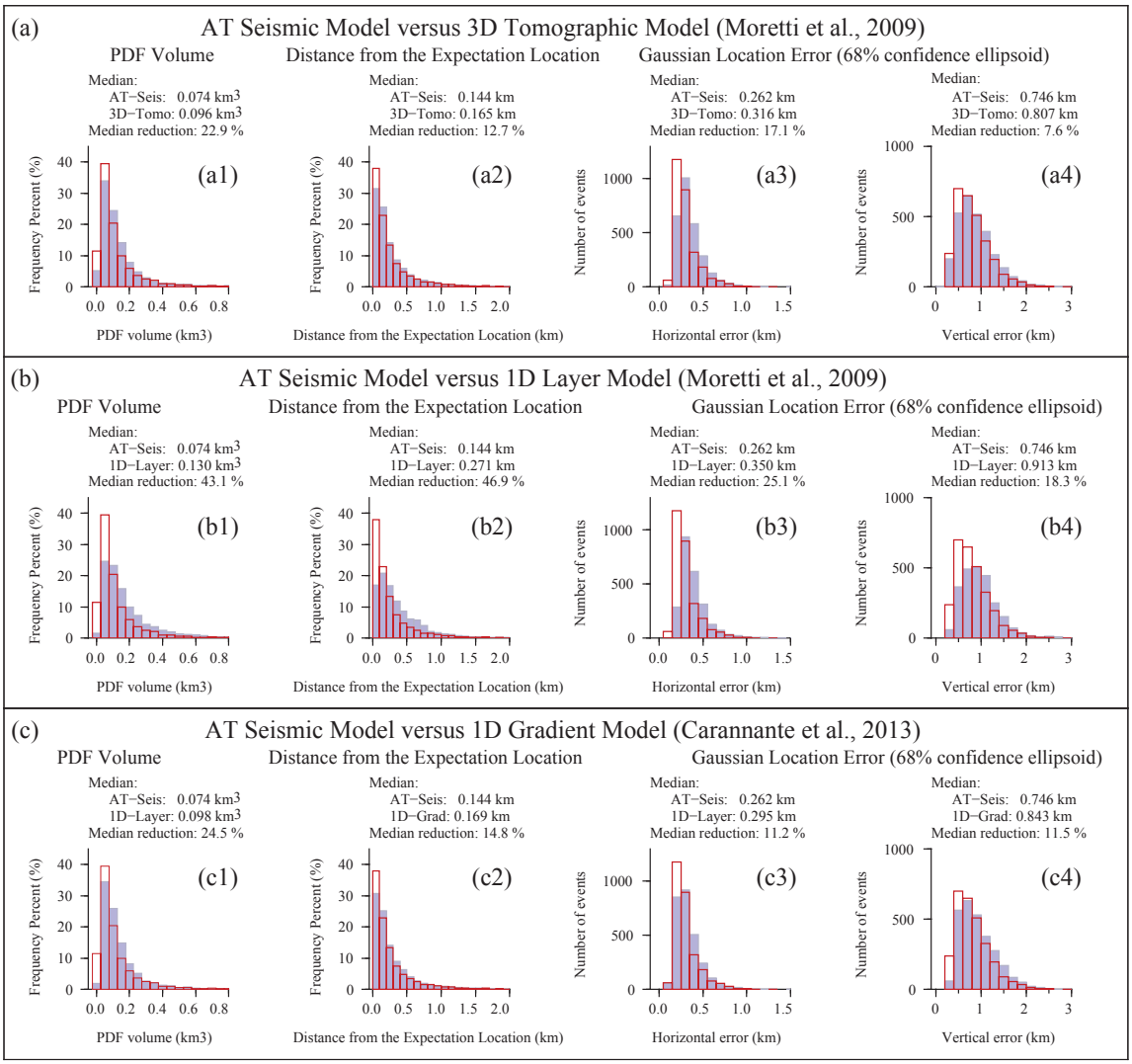
(a)
AT Seismic Model versus 3D Tomographic Model (Moretti et al., 2009)
PDF Volume
Median:
AT−Seis: 0.074 km3
3D−Tomo: 0.096 km3
Median reduction: 22.9 %
(a1)
Frequency Percent (%)
PDF volume (km3)
Distance from the Expectation Location
Median:
AT−Seis: 0.144 km
3D−Tomo: 0.165 km
Median reduction: 12.7 %
(a2)
Frequency Percent (%)
Distance from the Expectation Location (km)
Gaussian Location Error (68% confidence ellipsoid)
Median:
AT−Seis: 0.262 km
3D−Tomo: 0.316 km
Median reduction: 17.1 %
(a3)
Number of events
Horizontal error (km)
Median:
AT−Seis: 0.746 km
3D−Tomo: 0.807 km
Median reduction: 7.6 %
(a4)
Number of events
Vertical error (km)
(b)
AT Seismic Model versus 1D Layer Model (Moretti et al., 2009)
PDF Volume
Median:
AT−Seis: 0.074 km3
1D−Layer: 0.130 km3
Median reduction: 43.1 %
(b1)
Frequency Percent (%)
PDF volume (km3)
Distance from the Expectation Location
Median:
AT−Seis: 0.144 km
1D−Layer: 0.271 km
Median reduction: 46.9 %
(b2)
Frequency Percent (%)
Distance from the Expectation Location (km)
Gaussian Location Error (68% confidence ellipsoid)
Median:
AT−Seis: 0.262 km
1D−Layer: 0.350 km
Median reduction: 25.1 %
(b3)
Number of events
Horizontal error (km)
Median:
AT−Seis: 0.746 km
1D−Layer: 0.913 km
Median reduction: 18.3 %
(b4)
Number of events
Vertical error (km)
(c)
AT Seismic Model versus 1D Gradient Model (Carannante et al., 2013)
PDF Volume
Median:
AT−Seis: 0.074 km3
1D−Layer: 0.098 km3
Median reduction: 24.5 %
(c1)
Frequency Percent (%)
PDF volume (km3)
Distance from the Expectation Location
Median:
AT−Seis: 0.144 km
1D−Grad: 0.169 km
Median reduction: 14.8 %
(c2)
Frequency Percent (%)
Distance from the Expectation Location (km)
Gaussian Location Error (68% confidence ellipsoid)
Median:
AT−Seis: 0.262 km
1D−Layer: 0.295 km
Median reduction: 11.2 %
(c3)
Number of events
Horizontal error (km)
Median:
AT−Seis: 0.746 km
1D−Grad: 0.843 km
Median reduction: 11.5 %
(c4)
Number of events
Vertical error (km)

Figure 8. Figure

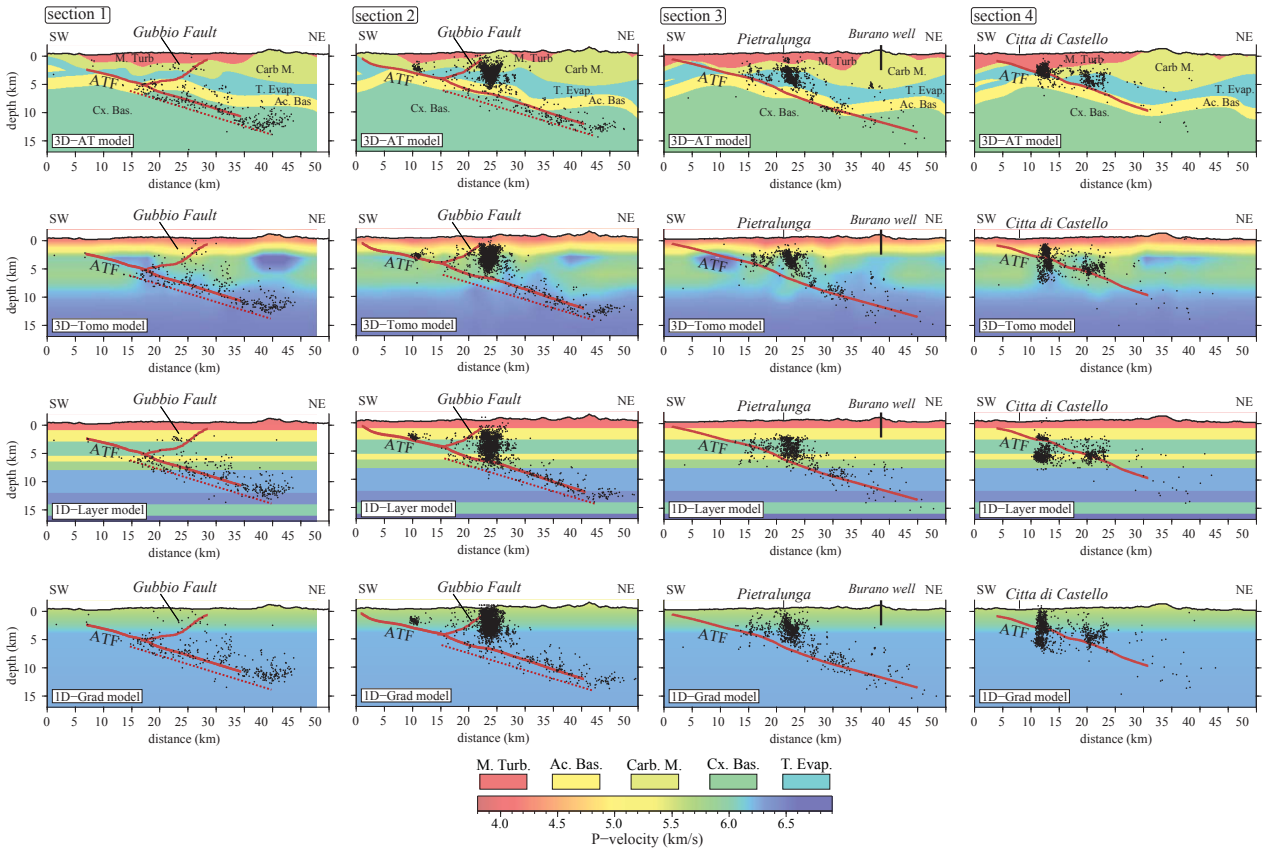
section 1
section 2
section 3
section 4
SW
NE
Gubbio Fault
Pietralunga
Burano well
Citta di Castello
M. Turb.
Carb M.
T. Evap.
Ac. Bas
Cx. Bas.
ATF
depth (km)
distance (km)
3D−AT model
3D−Tomo model
1D−Layer model
1D−Grad model
M. Turb.
Ac. Bas.
Carb. M.
Cx. Bas.
T. Evap.
4.0
4.5
5.0
5.5
6.0
6.5
P−velocity (km/s)

Figure 9. Figure

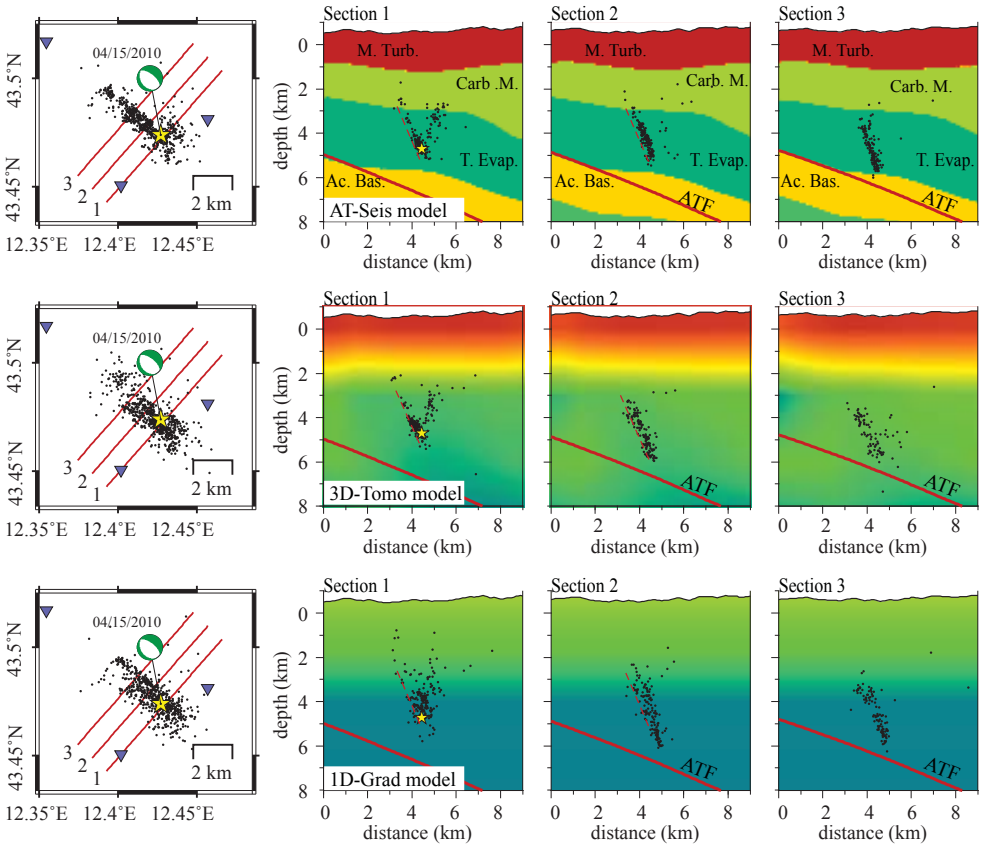
04/15/2010
43.5°N
43.45°N
12.35°E
12.4°E
12.45°E
2 km
1
2
3
Section 1
Section 2
Section 3
M. Turb.
Carb .M.
Carb. M.
T. Evap.
Ac. Bas.
ATF
AT-Seis model
3D-Tomo model
1D-Grad model
depth (km)
distance (km)
0
2
4
6
8

Table 1. Summary of seismic velocities from seismic reflection analysis, and in situ and laboratory measurements

Lithostratigraphic unit	**Average interval velocities** [*Mirabella et al., 2011*]	**Average velocities from in situ and laboratory measurements**	
	P-wave (km/s)	***P-wave (km/s)***	***Vp/Vs***
Miocene Turbidites	4.0	3.9	1.8
Carbonatic Multilayer	5.5	5.7	1.9
Triassic Evaporites	6.1	6.3	1.83
Acoustic Basement	5.1	5.3	1.72
Crystalline Basement *(only literature data)*	6.0 [*Ponziani et al., 1995*]	5.8 [*Burlini and Tancredi, 1998*]	1.81